FRONT MATTER

This is a non-peer reviewed preprint submitted to EarthArXiv. This manuscript has been submitted to *Science Advances* for publication.

Title

Australia's Tinderbox Drought: an extreme natural event likely worsened by human-caused climate change

Short Title

Australia's Tinderbox Drought

Authors

Anjana Devanand[1,2,*], Georgina M. Falster[3,4], Zoe E. Gillett[1,2], Sanaa Hobeichi[1,2], Chiara M. Holgate[3,4], Chenhui Jin[5,6], Mengyuan Mu[1,2], Tess Parker[5,6], Sami W. Rifai[1,2,7], Kathleen S. Rome[1,2], Milica Stojanovic[8], Elisabeth Vogel[1,9, 10], Nerilie J. Abram[3,4], Gab Abramowitz[1,2], Sloan Coats[11], Jason P. Evans[1,2], Ailie J. E. Gallant[5,6], Andy J. Pitman[1,2], Scott B. Power[5,6,12], Surendra P. Rauniyar[13], Andréa S. Taschetto[1,2], Anna M. Ukkola[1,2]

Affiliations

[1]ARC Centre of Excellence for Climate Extremes, University of New South Wales, Sydney, NSW, Australia.

[2]Climate Change Research Centre, University of New South Wales, Sydney, NSW, Australia.

[3]ARC Centre of Excellence for Climate Extremes, The Australian National University, Canberra, Australia.

[4]Research School of Earth Sciences, The Australian National University, Canberra, Australia.

[5]ARC Centre of Excellence for Climate Extremes, Monash University, VIC, Australia.

[6]School of Earth, Atmosphere and Environment, Monash University, VIC, Australia.

[7]School of Biological Sciences, University of Adelaide, SA, Australia.

[8]Centro de Investigación Mariña, Universidade de Vigo, Environmental Physics Laboratory (EPhysLab), Campus As Lagoas s/n, Ourense, 32004, Spain.

[9]Water Research Centre, School of Civil Engineering, University of New South Wales, Sydney, NSW, Australia.

[10]Melbourne Climate Futures, The University of Melbourne, Parkville, Victoria, Australia.

[11]Department of Earth Sciences, University of Hawai'i at Mānoa, Mānoa, United States of America.

[12]Centre for Applied Climate Sciences, University of Southern Queensland, Toowoomba, QLD, Australia.

[13]Australian Bureau of Meteorology, Melbourne, Australia.

***Corresponding author:** anjana.devanand@unsw.edu.au (AD)

Abstract

We examine the characteristics and causes of southeast Australia's Tinderbox Drought (2017–2019) that preceded the Black Summer fire disaster. The Tinderbox Drought was characterised by cool season rainfall deficits of around –50% in three consecutive years, which was exceptionally unlikely in the context of natural variability alone. The precipitation deficits were initiated and sustained by an anomalous atmospheric circulation that diverted oceanic moisture away from the region, despite traditional indicators of increased drought risk in southeast Australia generally being in neutral states. Moisture deficits were later intensified by unusually high temperatures, high vapour pressure deficits and sustained reductions in terrestrial water availability. Anthropogenic forcing intensified the rainfall deficits of the Tinderbox Drought by around 18% with an interquartile range of 34.9% to –13.3% highlighting the considerable uncertainty in attributing droughts of this kind to human activity. Skillful predictability of this drought was possible by incorporating multiple remote and local predictors through machine learning, providing prospects for improving forecasting of multi-year droughts.

Teaser

Australia's Tinderbox Drought was an unusually extreme natural event that was worsened by human-caused climate change.

MAIN TEXT

Introduction

Human-caused climate change is resulting in changes in the distribution of average rainfall across the globe, as well as amplification of the intensity of wet extremes and droughts (*1*, *2*). Warming over land is also driving an increase in atmospheric moisture demand that has the potential to further increase the likelihood and severity of droughts (*1*). Many regions have experienced an increase in observed drought intensity and frequency over the last few decades, particularly in mid-latitude regions of the northern and southern hemispheres, which support large proportions of the world's population and agricultural food security (*2*). There has also been an observed increase in compound events involving concurrent heatwaves with droughts (*1*). It is possible that drought characteristics are also changing, for example through the recently identified phenomenon of "flash droughts" that have rapid onset and intensification (*3*). At the same time paleo records identify multi-year to decadal "megadroughts" that were more intense and longer than any drought experienced during the instrumental period, indicating that far worse droughts are possible even without human-caused drought intensification. Future climate change simulations indicate droughts will intensify in many regions with global warming, and that every fraction of a degree of additional climate warming can worsen the severity and frequency of droughts in already drought-prone regions (*1*).

Despite the potentially devastating impact of droughts (*4*, *5*), the causes and predictability of individual drought events is usually poorly understood (*6*, *7*). This is partly because each event is unique and involves multiple interacting components of the climate system, and because the observational record provides very few examples of multi-year drought to study. Furthermore, current global climate models have limited skill in replicating multi-year droughts (*8*). Divergence of drought projections across multi-model ensembles also currently limits confidence in projected changes in many regions (*9*, *10*). The multifaceted nature and impacts of droughts means that these climate extremes cannot be adequately understood using single and standardised global metrics applied to observations or climate simulations. Instead, detailed analysis of high-impact case studies provides an alternate approach to advance our understanding of droughts.

Southeast Australia is a naturally drought-prone region and experienced a severe multi-year drought during 2017–2019. It was the driest three-year period since comprehensive instrumental records began in 1911 (*11*–*13*) and demonstrated the potential for drought events to contribute to cascading and compounding impacts across socio-economic and natural sectors (*14*). The 2017–2019 drought brought rural townships to the brink of running out of water (*15*), caused severe agricultural losses (*16*), and threatened the water supply of Australia's largest city, Sydney (*17*). The drought culminated in catastrophic forest fires in the spring and summer of 2019/2020 that burnt more than 5.8 million hectares of forest (*13*, *18*). The fires were unprecedented in the historical record for their spatial extent, radiative power, and the number of extreme pyroconvective events (*13*). We name the 2017–2019 drought the 'Tinderbox Drought', in recognition of the exceptional dryness of the event and how it preconditioned the region for unprecedented fire activity.

Some aspects of the development of the Tinderbox Drought were unexpected, raising urgent questions around why southeast Australia was in drought and how human-caused climate change might be increasing drought risk and/or altering drought predictability. In this paper we carry out a multidisciplinary assessment of the Tinderbox Drought in order to describe its characteristics, probability, drivers, and predictability. We use a broad range of observational sources, from in-situ measurements to global satellite-based products, as well as different modelling and machine learning approaches to illuminate key aspects of the Tinderbox Drought. We begin with a comprehensive description of the spatiotemporal characteristics of the drought, including impacts on hydrology, vegetation and agriculture. We then assess how unusual the drought was in the context of observational data, followed by an exploration of the physical mechanisms that led to the extreme and sustained precipitation deficits. Finally, we assess the predictability of the drought and how unusual the drought was in the context of simulated long-term climate variability and what role climate change may have played in exacerbating it. We conclude by drawing together the multifaceted analysis of the Tinderbox Drought, and the insights this event gives for droughts in a warming world.

Results

Characterisation and impacts of the drought

We begin by identifying the temporal and spatial characteristics of the Tinderbox Drought. Droughts commonly start as a precipitation deficit (meteorological drought), which propagates to other components of the surface water cycle including streamflow and water storages (hydrological drought), soil moisture and plant water stress (agricultural and ecological drought). While deficits in precipitation are an obvious driver of droughts, the development and intensification of droughts are also influenced by temperature, radiation, wind, and humidity that alter atmospheric evaporative demand. For example, the increased presence of high-pressure weather systems (anticyclones) during droughts in southeast Australia reduces cloud cover, increasing the local incoming radiation. These changes affect land-atmosphere feedbacks, reducing rainfall recycling in some regions which can intensify precipitation deficits (*19*, *20*). Further, soil moisture deficits reduce evaporative cooling, increasing air temperatures through increased sensible heating, increasing evaporative demand and thereby further depleting soil moisture via a positive feedback loop.

Here, we use drought metrics (see Materials and Methods) based on precipitation, potential evapotranspiration and soil moisture to identify the focus region of the Tinderbox Drought. The impact of the drought in this region is then characterised by examining water, atmospheric, vegetation, and agricultural datasets.

The drought focus region

The Australian Bureau of Meteorology describes precipitation deficits during the 2017–2019 drought as primarily occurring during the cool season months of April to September (*11*). Focusing on the cool season months and using a combination of drought metrics (SPI-3 and SPEI-3, see Materials and Methods) from multiple datasets, we calculate the spatial pattern of time spent in drought during the Tinderbox Drought (Fig. 1, Fig. S1A). Areas of southeast Australia between 25-35°S, and east of 137°E were commonly (>50% of the time) in drought during the cool seasons of 2017–2019. Consistent results are found when repeating this analysis using all months of 2017–2019 (Fig. S1B). The identified drought region is further consistent if simple rainfall thresholds (Fig. S1C-D), or a threshold approach based on soil moisture data (Fig. S1E-F) are used.

We therefore define the Tinderbox Drought region (Fig. 1) based on these consistent spatial patterns of the proportion of time in drought derived from different assessment methods (Fig. S1). The boundaries of the Tinderbox Drought region show a strong correspondence with the Murray-Darling Basin (MDB). The drought affected virtually all of the New South Wales and southern Queensland parts of this major drainage basin and the agricultural land it supports (Fig. 1A). Sustained cool-season drought over the full 2017–2019 interval was not evident along the coastal fringe of eastern Australia or the majority of Victoria, although some of these regions did experience drought impacts during some parts of the Tinderbox Drought. This is particularly true for the final year of the drought (2019) when most of southeast Australia experienced exceptionally dry conditions that were sustained throughout almost the full year (Figs. S2 and S3), including the forested coastal and mountain regions of southeast Australia where the subsequent Black Summer fires were concentrated. The region defined here for the Tinderbox Drought (Fig. 1) is used throughout this study.

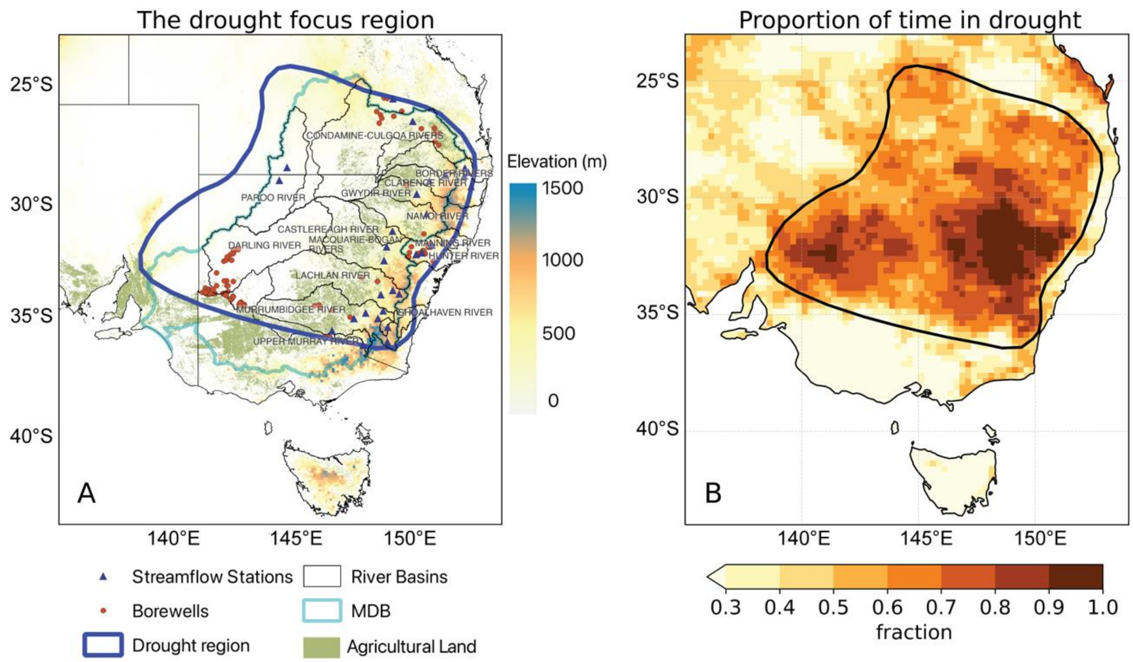

Fig. 1. The drought focus region (**A**) Thick blue line shows the outline of the region in drought during 2017-19. Basemap colours denote elevation. The map also shows agricultural areas, the Murray Darling Basin (MDB - thin aqua line), smaller river basins, locations of streamflow stations and borewells, (**B**) the proportion of time in drought during April to September 2017-19 based on standardised drought metrics. Thick black line denotes the drought area. The fraction of time spent in drought is calculated here as the mean proportion of time SPI-3/SPEI-3 $\leq$ -1 for data encompassing only the cool season months (April-September) of 2017-19 based on three precipitation and two PET datasets (Materials and Methods; Fig. S1)

Temporal evolution of the water cycle during the drought

Area-mean precipitation anomalies over the Tinderbox Drought region show sustained rainfall deficits throughout 2017–2019, indicative of meteorological drought (Fig. 2A). Precipitation was below the 1980–2016 baseline for 31 out of the 36 months in 2017–2019. Rainfall deficits during the cool seasons of these three years were about –50% (ranging from –46% to –56%). Summer precipitation was also substantially reduced, with deficits of –27% in 2016/17, –26% in 2017/18 and –54% in 2018/19. Sustained and intensifying rainfall deficits during 2017 resulted in the majority of New South Wales moving into drought watch conditions from mid-2017, and by October of 2017 drought conditions had become established in some regions (*21*). In some regions the drought also involved rapid intensification as a flash drought (*22*). The intense rainfall deficits of the Tinderbox Drought also form part of a multi-decadal dry interval over southeast Australia, where 15 of the previous 20 years (2000–2019) recorded rainfall below the long-term average (*13*).

Monthly evapotranspiration (ET) anomalies during the Tinderbox Drought (Fig. 2A) show very similar patterns to monthly precipitation anomalies but ET deficits intensified as the multi-year drought progressed. The average cool season ET deficit during 2017 was –24% while all months of 2018 had negative ET anomalies that ranged from –22% to –49%. The largest deficits in ET occurred in 2019, with monthly anomalies during all months except autumn (MAM) ranging between –41% to –57%. Using P minus ET (P-ET) as a measure of water availability, average deficits ranging from –5 to –15 mm $month^{-1}$ occurred during the cool seasons and summers of 2017–2019. These negative water availability anomalies contributed to strong declines in water stores and streamflow (Fig. 2C-E).

Maximum air temperatures and atmospheric dryness were exceptionally high during the Tinderbox Drought, culminating in several severe heatwaves that further intensified the drought conditions and fire risk (*13*, *23*). Maximum temperature (T_{max}) over the drought region was above the 1980–2016 average throughout the Tinderbox Drought (Fig. 2B). The mean 2017–2019 anomaly was 1.6°C, and of the 36 months in 2017–2019, 35 of them had positive T_{max} anomalies, with the largest anomalies over summers (1.8 to 2.8°C). This region has experienced anthropogenic warming over the 20th century and the 1980-2016 baseline used here is 0.3°C above the 1911–1940 mean T_{max}. The exceptional heat during the Tinderbox Drought differentiates this event from previous drought events in southeast Australia that have typically been associated with temperatures around 1.0°C above the long-term mean (*11*).

A significant inverse relationship between monthly precipitation and T_{max} anomalies existed over the Tinderbox Drought region during 2017–2019 (Fig. 2A-B) with months with higher temperature anomalies coinciding with months of greater precipitation deficits ($r = –0.39$, $p<0.05$). The observed monthly covariance between temperature and precipitation anomalies is also a robust feature of the longer term interannual climate variability of this region (*13*).

Vapour pressure deficit (VPD), a measure of the ability of the atmosphere to take up water from the surrounding landscape, is an important indicator of ecological stress. The area-averaged afternoon VPD anomalies in the drought focus region were consistently positive throughout the period from summer of 2016/17 to summer of 2019/20, indicating an enhanced deficit in atmospheric moisture relative to saturation capacity (Fig. 2B). Between November 2016 and January 2020, 34 of the 39 months experienced VPD anomalies greater than the 2002–2016 baseline mean. We estimate VPD anomalies here from a shorter baseline for consistency with assessments using satellite based vegetation datasets (Fig. 3). Seasonal anomalies in VPD during the Tinderbox Drought ranged from 2% to 25%, with some monthly anomalies exceeding 30%.

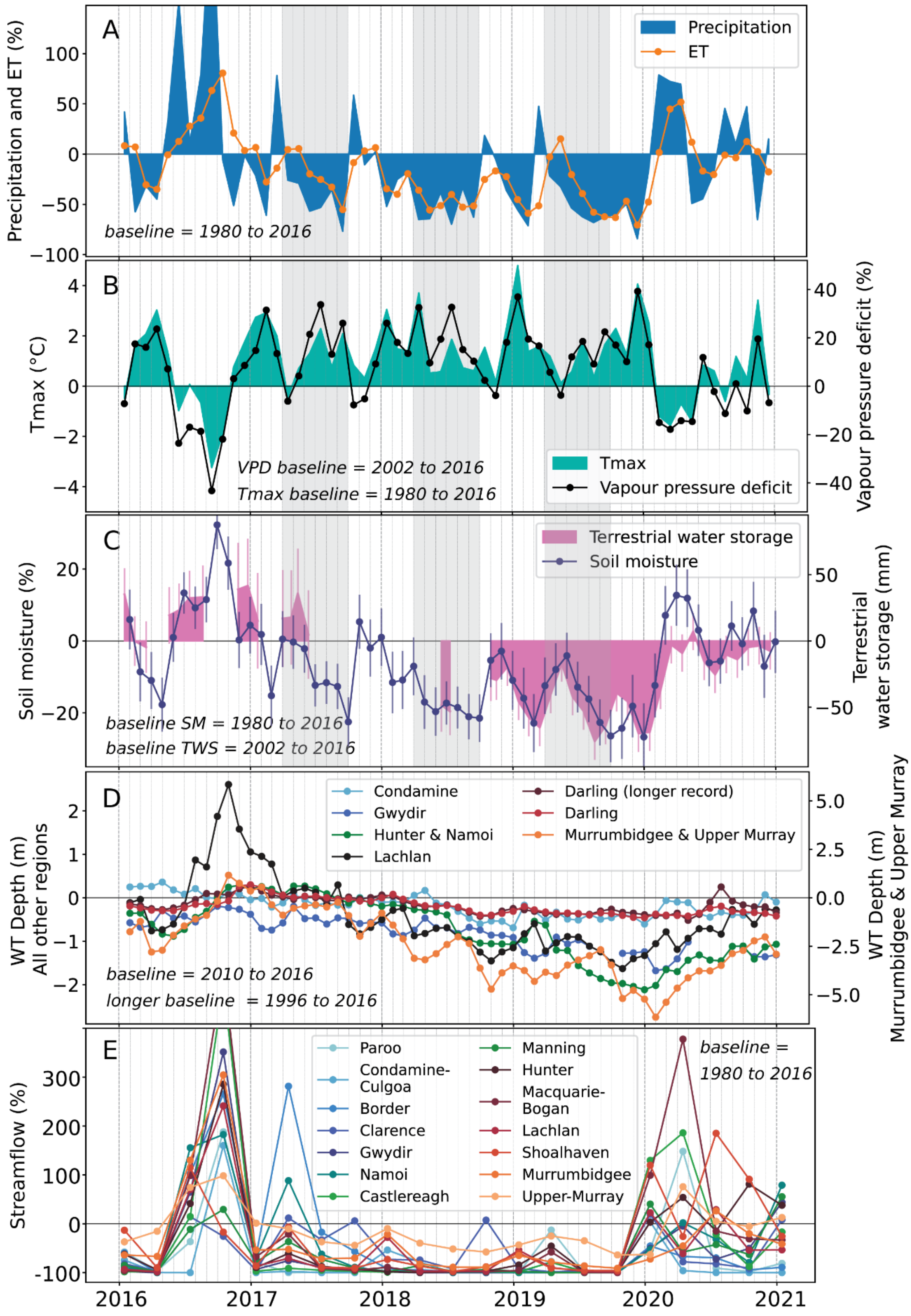

Fig. 2. Monthly anomalies in water cycle components in the drought focus region. (**A**) Precipitation and evapotranspiration (ET) (%), (**B**) vapour pressure deficit (%), and Tmax (°C) (**C**) soil moisture from the European Space Agency dataset (%), and terrestrial water storage from GRACE data (mm). (**D**) Monthly anomalies in water table depth (m) from bore well data. The water level anomalies in the

Murrumbidgee and Upper Murray are shown on the right y-axis. (**E**) Seasonal anomalies in streamflow (%). Anomalies are calculated with respect to a baseline (1980–2016), unless constrained by data availability. The figure shows the period covering one year before and after the drought (2016–2020), and vertical shading in panels A-C indicates the cool seasons of the Tinderbox Drought.

Surface and groundwater datasets demonstrate the progressive worsening of hydrological drought during 2017–2019 (Fig. 2C). During 2017, surface soil moisture was on average –6% (and –11% during the cool season), with 8 months experiencing soil moisture levels below the 1980–2016 mean. During 2018 and 2019 all months experienced negative soil moisture anomalies. The average soil moisture anomaly in 2018 had intensified to –14%, and in 2019 intensified again to –17%. By 2019, these moisture deficits amounted to around a 50mm lowering of terrestrial water storage (below the 2002–2016 mean). Interestingly, drought monitoring in NSW saw drought indicators from soil moisture and plant growth deficits appear several weeks ahead of the rainfall deficits indicative of drought during both the onset of the drought in 2017 and the drought intensification in 2019 (*13*).

Water table depths measured in borewells also showed progressive declines through the drought (Fig. 2D). Water levels were at or above climatology at the start of 2017 and declined near continuously to reach peak deficits at the end of 2019/early 2020. Maximum deficits in water table depth ranged between –0.4 to –0.6 m in the Darling and Condamine basin regions, –1.3 to –2.1 m in the Gwydir, Hunter and Namoi and Lachlan basin regions, and –6.1 m in the Murrumbidgee and Upper Murray basin region.

Streamflow in the drought focus region is highly variable. Large negative flow anomalies are typically recorded during most of the seasons in the historical record (~60–70% of seasons), and these deficit seasons are interspersed with small clusters of seasons with large positive flow anomalies. Due to this high short-term variability, we use seasonal rather than monthly anomalies to characterise the changes in streamflow during the Tinderbox Drought (Fig. 2E). In most basins, large positive streamflow anomalies were recorded in winter and spring of 2016 ahead of the initiation of the Tinderbox Drought. Seasonal flows declined variably across the different catchments during 2017, with more intense, widespread and sustained reductions in flow during most of 2018 and 2019. The average flow anomalies during the 2018 cool season of the Tinderbox Drought ranged from –82% to –100% (i.e. no flow) in all basins except the Upper Murray (–51%) where flows are less variable than in the other basins. By the spring (SON) of 2019, the flow anomaly in the Upper Murray had declined to –64%, and to –91% to –100% in other basins.

The Tinderbox Drought ended with positive precipitation anomalies during February to April 2020, which were also accompanied by negative T_{max} and VPD anomalies. Soil moisture across the drought region returned to positive anomalies in February 2020, and terrestrial water storage recovered by around March 2020. In the summer of 2019/20, some river basins within the drought region recorded positive streamflow anomalies as a result of heavy rainfall in February, followed by a recovery of streamflow in other basins later in 2020. An exception to this was the Border and Condamine-Culgoa river basins in the northern part of the drought focus region, where negative streamflow anomalies persisted through to the end of 2020. Water table anomalies demonstrate a much slower recovery from the impacts of the Tinderbox Drought. Although positive water table trends were seen from early 2020, negative anomalies persisted in all basins until at least mid-2020. By the end of 2020, nearly a year after the drought-breaking rainfall that ended the meteorological drought, negative water table anomalies of –1 to –1.3 m still remained in the Gwydir, Hunter and Namoi basins and about –2.9 m in the Murrumbidgee and Upper Murray basin regions.

The impact of the drought on vegetation

Sustained soil moisture and VPD anomalies and the resulting impacts on vegetation were a defining feature of the Tinderbox Drought and subsequent Black Summer fires. A key difference between the Tinderbox Drought and earlier major droughts in southeast Australia were the sustained high VPD anomalies (Fig. 2B, Fig. 3), which likely exacerbated the drought's impact on vegetation. Soil moisture droughts reduce the water supply to plants, whereas atmospheric droughts (anomalously high VPD) increase the atmospheric demand for water from the plant. Plants generally respond to increasing VPD by closing stomata (*24*), which reduces photosynthesis and transpiration. The reduction of transpiration reduces latent cooling causing leaves to heat up and potentially exceed their photosynthetic optimum temperature. Even if plants shed leaves to reduce water loss, the lack of soil moisture and the high VPD can still lead to serious impacts (*25*). High VPD can also increase fuel dryness and increase fire risk (*26*).

During the Tinderbox Drought, an annual mean VPD anomaly in excess of 10% was sustained throughout the three-year duration of the drought (Fig. 3A). VPD is also seen to progressively intensify through the drought, suggesting a role in sustaining and intensifying the drought conditions. In contrast, the Millenium Drought only had a 10% VPD anomaly during a single year, 2002, and did not show a sustained increase in VPD through the drought event (Fig. 3A). However, we do note that the Millennium Drought was focused on the southern MDB (primarily Victoria) and did not affect the full study area assessed here for the Tinderbox Drought. Previous work has demonstrated that there has been a sustained positive trend in VPD over southeast Australia, such that during the Tinderbox Drought the long-term VPD conditions had emerged outside of the range of historical (1950–1999) experience (*13*).

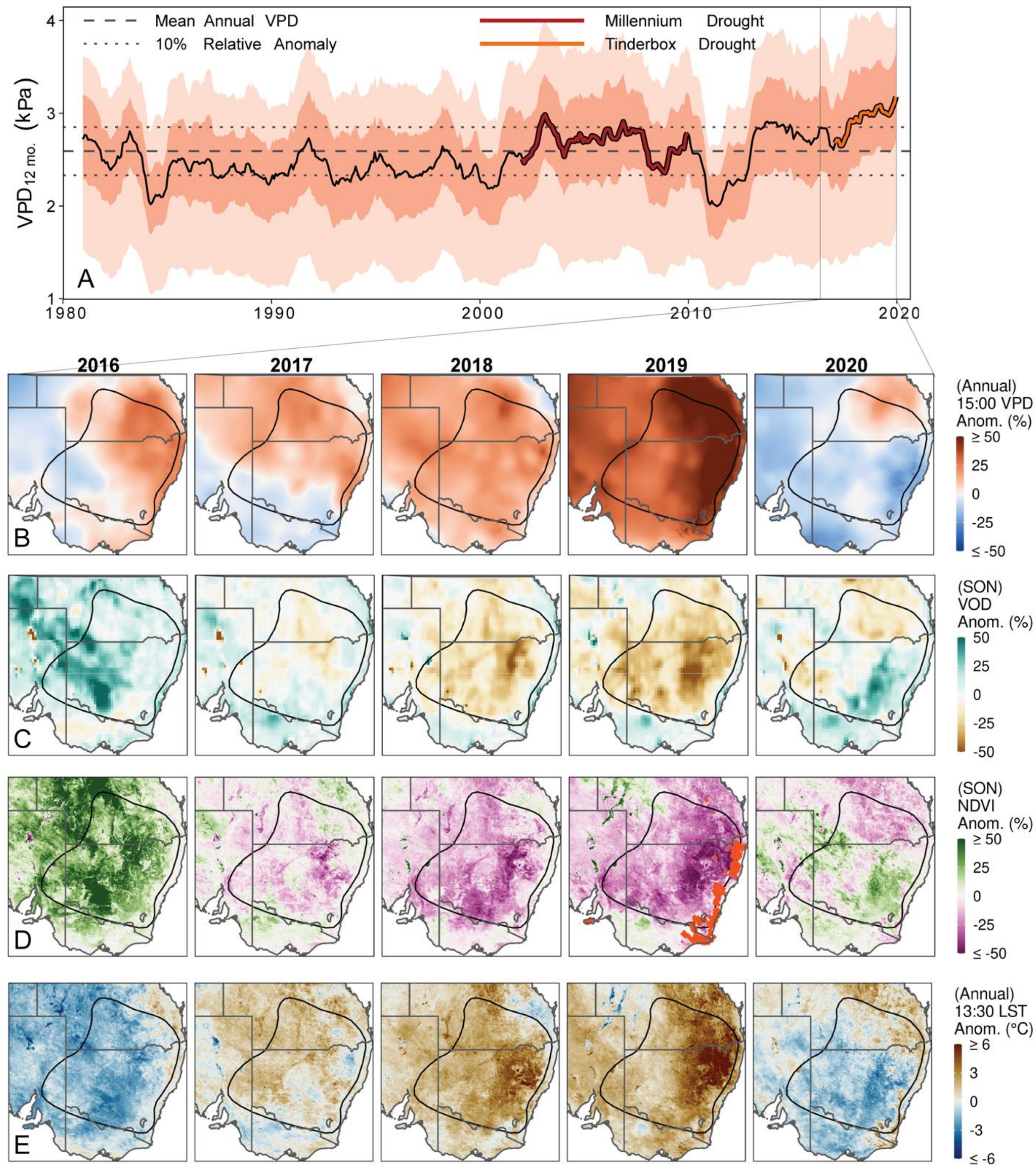

Fig. 3. The evolution of the drought impacts on vegetation in southeast Australia. (**A**) The 12-month rolling mean of vapour pressure deficit (VPD; 15:00 hours reading from AGCD) across the focal region is shown for 1981–2020. The shadings show the inner 50% and 90% range of the focal region's VPD. The mean annual VPD and 10% deviation are overlaid. The Millennium and Tinderbox droughts are highlighted. (**B**) The relative vapour pressure deficit (VPD) anomaly expressed as a percent deviation from the 2002–2016 mean annual value. (**C**) The relative anomaly of the vegetation optical depth (VOD) during SON is plotted as a percent deviation from the 2002–2016 SON seasonal mean. (**D**) The relative anomaly of the Normalized Difference Vegetation Index (NDVI) is plotted as a percent deviation from the 2002–2016 seasonal SON mean. Regions that experienced burning during the 2019 Black Summer fires are denoted by orange points. (**E**)

The annual mean of the daytime (13:30 overpass time) land skin temperature anomaly (LST; °C) as derived from the MODIS AQUA platform.

There was also a distinct spatial evolution of VPD anomalies during the Tinderbox Drought (Fig. 3B). In 2016, VPD was already high over the northeastern half of the drought region, indicating the potential for ecological stress to increase before the soil moisture deficits across the region developed (Fig. 2C). Positive VPD anomalies became more widespread and intense throughout the Tinderbox Drought, so that by 2019 VPD was between 25–50% higher than average over the entire region (Fig. 3B).

A clear progression of vegetation stress also occurred during the Tinderbox Drought, which we illustrate for spring (SON) of each year (Fig. 3C-D). Vegetation Optical Depth, a remote sensing proxy of plant canopy moisture content, was high in 2016 but was followed by an accumulation of increasingly negative anomalies as the Tinderbox Drought developed and intensified through to the end of 2019 (Fig. 3C). This effect can also be seen using the Normalized Difference Vegetation Index (NDVI), a long established proxy of canopy leaf area (Fig. 3D). In 2016 there were widespread positive NDVI anomalies (i.e. higher canopy area), but this was followed by a precipitous drop in the subsequent drought years. By spring of 2019 more than 96% of the drought region experienced negative NDVI anomalies, with a mean anomaly of –22% (Fig. 3D). The lack of plant moisture and canopy area reduced evaporative cooling over the drought region. This is evident via the close correspondence of the spatial distribution and intensity of NDVI and surface temperature anomalies during the Tinderbox Drought, leading to an increase of land surface temperatures as the drought progressed (Fig. 3E).

Agricultural impacts during the drought

Australia is one of the top ten producers and exporters of wheat, barley and cotton worldwide. Australian wheat accounts for almost 10% of global wheat trade, amounting to a 2018–2021 average export value of 5.3 billion AUD (*27*). Australian barley production accounts for 30–40% of the world's malting barley trade and 20–30% of global feed barley trade amounting to a 2017–2021 average export value of 2 billion AUD (*28*). Southeast Australia is the major centre for this agricultural production, providing around 40% of the nation's total agricultural output.

The impacts of the Tinderbox Drought on wheat and barley production across the drought-affected region were considerable, especially in the second and third year of the drought (Fig. S4). Wheat and barley are winter crops and predominantly rainfed, leading to high sensitivity to interannual variations in cool season rainfall. Wheat production in 2018 and 2019 dropped by 73% and 63%, and barley production dropped by 47% and 43% compared to the 1990–2016 average. Wheat showed negative yield anomalies in all three years of the drought. Within the observation period for which yields at sub-national scale are available (starting in 1990), negative yield anomalies over three or more years have only been seen previously during the Millennium Drought (in 2002–2004 and 2006–2009). Similarly, barley exhibited negative yields in two consecutive years (2018 and 2019), which had only been observed once before in 2006–2007 of the Millennium Drought.

Agricultural production data for rice and cotton are only available at a national scale, however the major production areas for these crops occur within the focus region of the Tinderbox Drought. Rice and cotton are irrigated summer crops with a growing season ranging from spring to autumn, and are particularly vulnerable to reduced availability of irrigation water. Rice was the most negatively affected of all four assessed crops, with reductions in rice production of more than 90% in the 2018/19 and 2019/20 growing seasons, compared to the long-term 1990–2016 average (Fig. S4C). These production losses were driven by strong decreases in the area harvested, which was reduced by 92%–95% in 2018/19 and 2019/20. The area used for cotton in 2018–19 dropped to 10% below the long-term average, and production reduced to a +12% anomaly, down from +71% in the previous year. Severe decreases in cotton production were then seen in the 2019/20 growing season when cotton production dropped to –74% compared to the 1990–2016 average, the lowest value since 1982/83. This drop was driven by a strong reduction in the harvested area to –79% compared with the long-term mean.

The production data underline the severity of the Tinderbox Drought for agricultural producers in southeast Australia. The impacts of meteorological drought appear to be particularly evident for wheat and barley production, which were impacted by deficits in cool season rainfall particularly in 2018 and 2019 (Fig. 2A, Fig. S4A-B). Since rice and cotton are irrigated crops, their production is strongly linked to access to irrigation water and fluctuations in water markets. These irrigated crops appear to have been impacted primarily by the intensification of hydrological drought as the Tinderbox Drought progressed causing extreme water table and streamflow deficits by 2019 (Fig. 2D-E, Fig. S4C-D).

Probability of drought occurrence

The Tinderbox Drought involved extreme and sustained precipitation deficits, but how unusual were these in the context of natural climate variability? It is well established that the short length of the observational rainfall record in southeast Australia is insufficient to capture the full possible range of natural hydroclimatic variability (*29*, *30*). To address this limitation and test how unusual the three sequential years of 2017–2019 were, we use two complementary approaches. Firstly, we assess randomly resampled 3-year anomalies of cool season rainfall using the 1900–2019 observed rainfall data for the drought focus region. Secondly, we use Linear Inverse Models (LIMs) as an empirically-based null hypothesis for the observed precipitation deficits occurring due to internal climate variability (Materials and Methods; Fig. 4).

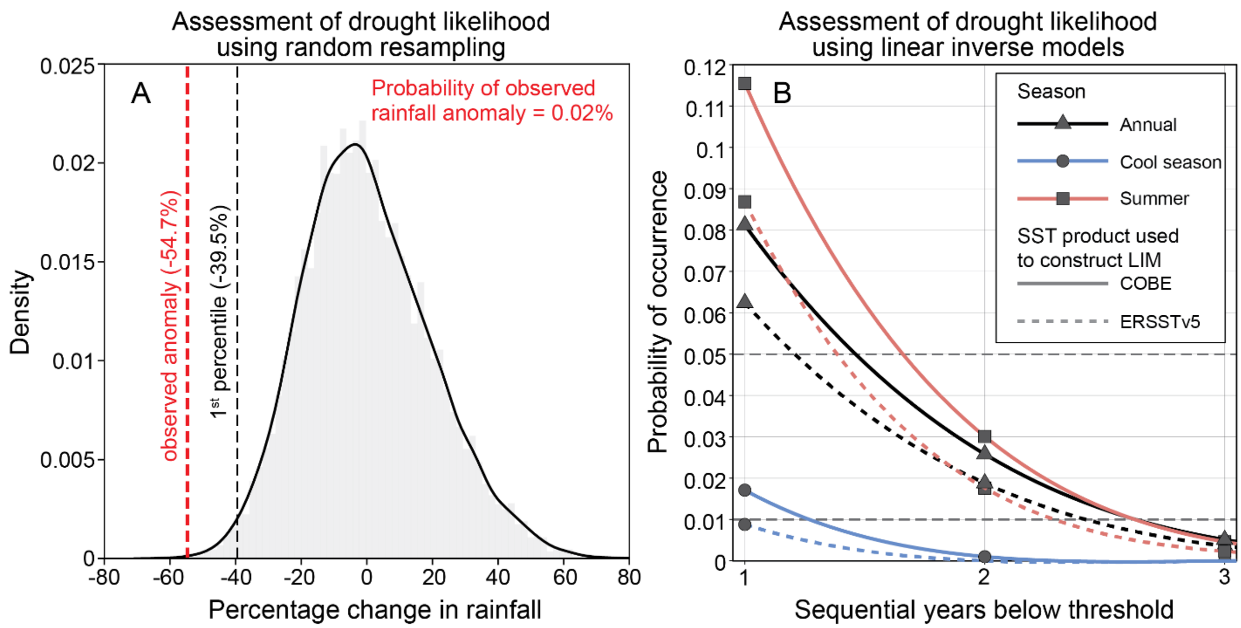

Fig. 4. Probability that the 2017–2019 southeastern Australian meteorological drought occurred within the range of internal variability. (**A**) The observed deficit in cool season (AMJJAS) rainfall of the Tinderbox Drought (2017–2019; red dashed line) relative to the first 60 years of the observational period (1900–1959). The likelihood of the observed 2017–2019 rainfall deficit is assessed relative to random resampling of the full historical period (1900–2019) 10,000 times and computing the precipitation anomaly of the last 3 years compared to the first 60 years of the resampled data (grey shaded distribution). The black dashed line indicates the 1% significance level based on the bootstrapping relative frequency distribution. (**B**) Probability of occurrence of the least severe annual (black), cool season (AMJJAS; blue), and summer (DJF; salmon) precipitation deficit observed during the 2017–2019 drought, for one, two, and three sequential years as estimated from the LIMs. The solid line shows the distribution constructed using SST data from COBE, and the dotted line shows the distribution constructed using SST from ERSSTv5. Dashed horizontal grey lines show 5 % and 1 % significance levels.

The likelihood of 3-year cool season rainfall deficits equivalent to what occurred during the Tinderbox Drought is exceptionally low (Fig. 4A). Random resampling of individual years (with replacement) from the full observational rainfall record for the drought region demonstrates that the observed Tinderbox Drought anomalies were at the 0.02% level of 10,000 random rearrangements of the historical record. This suggests that the likelihood of the observed 2017–2019 cool season rainfall deficits happening due only to natural climate variability was exceptionally low.

The precipitation deficits of the Tinderbox Drought were also exceptionally unlikely when assessed against an empirically-based null hypothesis (Fig. 4B). Unlike the random resampling of observed precipitation (Fig. 4A), the LIM precipitation trajectories maintain temporal autocorrelations (Materials and Methods). This allows assessment of the temporal evolution of the drought, and how unusual this was in the context of mostly ocean-forced internal climate variability. The probability of experiencing a single-year cool season precipitation deficit equal to that of 2017—the least severe year of the Tinderbox Drought—was between 0.9% and 2%. The full annual precipitation deficit for 2017 had a likelihood of 6–8%. Expanding the assessment to examine sequential precipitation deficits at least as severe as 2017 demonstrates an increasingly low likelihood (Fig. 4B). Three sequential years of cool season deficits at least as severe as 2017 are outside the range of simulated variability, occurring at a rate of 0% in the LIM simulations. The observed Tinderbox Drought was even more severe than this, given 2017 had the least dry cool season of the three drought years. Three sequential years of annual and summer deficits at least as severe as the least dry year of the drought are also extremely unusual (< 1%) within the range of internal precipitation variability.

Together these assessments indicate that the likelihood of experiencing a meteorological drought as severe as the 2017–2019 event is much less than 1%, if we assume that the event and the historical record were wholly driven by internal climate variability. This means that the Tinderbox Drought was either an exceptionally rare natural event, or that anthropogenic forcing played a role in exacerbating this drought.

Mechanisms driving the drought

Large-scale climate drivers

Australia's highly variable rainfall is frequently linked to large-scale modes of climate variability. Dry conditions in southeast Australia are commonly associated with El Niño or positive Indian Ocean Dipole (IOD) events, while the Southern Annular Mode (SAM) causes differing rainfall impacts between the cool and warm seasons. The state of these modes of variability contribute to long-range (seasonal) rainfall outlooks, and previous major multi-year droughts in southeast Australia have been linked to these drivers. For example, the Federation Drought (1895–1902) has been linked with high El Niño activity and a positive phase of the Interdecadal Pacific Oscillation (*31*), while the World War II Drought (1937–1945) has been related to cool sea surface temperatures in the eastern Indian Ocean (*31*). The Millennium Drought (or Big Dry, 1997–2009) was influenced by a positive SAM phase, and a series of Central Pacific El Niño events (*31*, *32*). Recent work has also highlighted the importance of the rain-promoting phases of the modes of variability — specifically La Niña and negative IOD events — in ending droughts over southeast Australia (*33*–*35*).

Large-scale ocean variability played some role in driving rainfall deficits during the Tinderbox Drought, although with notable differences to the large-scale modes of variability that have commonly been used to assess the drivers of past droughts. Interannual rainfall variability during April to September in the Tinderbox Drought region is significantly correlated with sea surface temperature (SST) in the tropical oceans around northern Australia (Fig. 5A,C; r = 0.77 for the region 5–20°S, 100–160°E; see also (*36*, *37*)). Within this broad tropical ocean region to the north of Australia, correlations are highest in the eastern Indian Ocean and Coral Sea sectors (Fig. 5A). The correlation strength between the ocean north of Australia and cool season rainfall anomalies over the drought region surpasses those from the traditional El Niño Southern Oscillation (ENSO) indices commonly used to inform seasonal outlooks of rainfall, i.e. Niño3.4 index (r = –

0.52; Fig. 5E), Niño4 index (r = –0.54; Fig. 5D), and the Southern Oscillation Index (r = 0.58).

ENSO was neutral in April-September of 2017, developed into a weak and short-lived La Niña by the end of 2017, and returned to neutral conditions by mid-2018 (Fig. 5F). The sign and strength of the tropical Pacific SST suggest that ENSO was unlikely to have promoted the large rainfall anomalies in southeast Australia at the start and intensification of the drought. A weak Central Pacific El Niño developed in late 2018 and persisted through winter 2019 (Fig. 5F, blue line), and has been suggested to have contributed to the cool season rainfall deficits of the final year of the Tinderbox Drought (*38*) and into the Black Summer of 2019/20. However, the absence of sustained and/or strong El Niño conditions during the Tinderbox Drought suggests that ENSO was not a major driver for this drought, despite the longer-term importance of tropical Pacific climate variability for rainfall in eastern Australia in both the cool and warm seasons (Fig. 5D-E; Fig. S5).

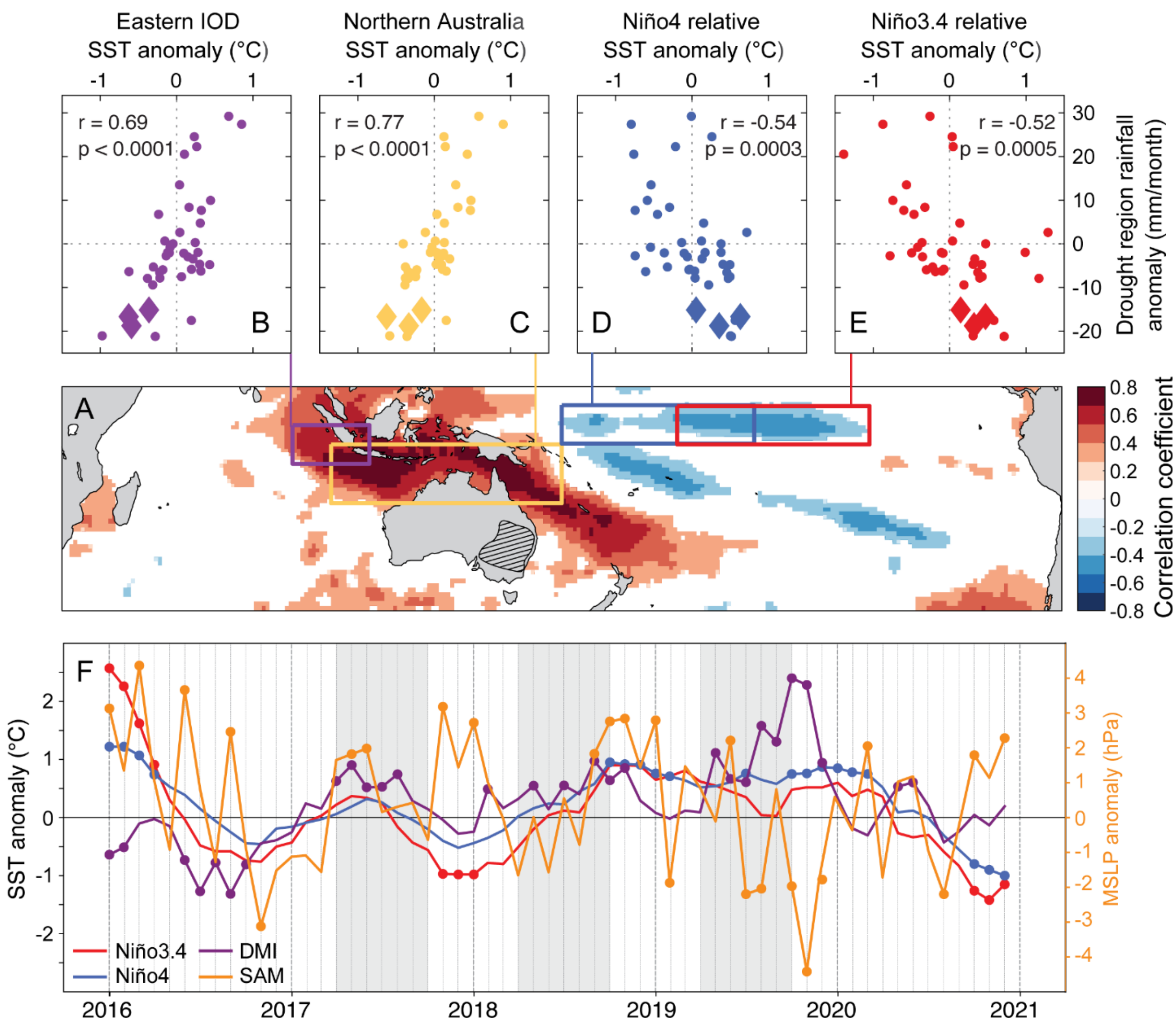

Fig. 5. Sea surface temperature and large-scale influences on rainfall in the Tinderbox Drought region. (**A**), Spatial correlation of April-September rainfall anomalies in our study region (hatching) with SST anomalies, showing only correlations significant at p < 0.1. Coloured boxes show the southeast tropical Indian Ocean (purple, 0–10°S and 90°–110°E), northern Australia (orange, 5°–

20°S and 100°–160°E), Niño4 (blue, 5°N–5°S and 160°E–150°W) and Niño3.4 (red, 5°N–5°S and 120°–170°W) regions explored further in B-E. (**B-E**), relationship between rainfall anomalies in our study region with SST averaged over regions indicated in A, for April–September anomalies between 1982–2020 (circles), with the 2017–2019 Tinderbox Drought years indicated by diamonds. Data in this figure uses the OISST v2 0.25°×0.25° SST product and the ACGD rainfall product (Methods). All data in A-E are linearly detrended to isolate interannual variability and the Niño3.4 relative index (D) is calculated by first removing the tropical ocean mean (*39*). Anomalies in B-E are relative to 1982–2016 climatology (Methods). (**F**), Time series of the Niño3.4 (red), Niño4 (blue), DMI (purple) and SAM (orange) indices between 2016–2020. Months that exceed one standard deviation of the respective index (computed over 1980–2016) are indicated with markers. Grey shading denotes the cool seasons of the Tinderbox Drought.

The IOD was weakly positive in April-September of 2017 and 2018, and a record positive IOD event occurred in 2019 (Fig. 5F), promoting below-average winter-spring rainfall in southeast Australia (*13*). The relationship with the Dipole Mode Index (DMI) and cool season rainfall in our study region ($r = -0.61$) is dominated by SST anomalies in the eastern pole used for the DMI ($r = 0.69$, Fig. 5A-B). SSTs in the eastern IOD region were consistently below their climatological mean for all three years of the Tinderbox Drought. Previous studies have suggested that cool SST anomalies in the eastern Indian Ocean (and the absence of warm SST anomalies from negative IOD events) were more important than tropical Pacific Ocean conditions in establishing and sustaining previous major droughts in southeast Australia (*33*). Our findings suggest that the importance of eastern Indian Ocean SST anomalies also held true for the Tinderbox Drought.

The three years of the Tinderbox Drought were characterised by cool SST anomalies across widespread areas in the eastern Indian Ocean and Southern Ocean (Fig. S6). These cool SST anomalies continued to intensify and spread further east from 2017 to 2019, such that by April–September of 2019 almost all of the ocean area around Australia was below average. The exception to this was the warm SST anomalies that persisted off eastern Australia, adjacent to the drought region. The synoptic processes that help explain the observed connections between remote SST anomalies, moisture transport and rainfall anomalies during the Tinderbox Drought are investigated in the subsequent sections.

In addition to tropical climate drivers and their associated SST anomalies, rainfall variability in southeast Australia is also influenced by atmospheric variability of the SAM. The positive phase of the SAM (poleward shift of the midlatitude jet) is associated with decreased rainfall over parts of southern and eastern Australia during the cool season (*40*). However, no significant relationship is evident in the correlation of the cool season SAM with rainfall anomalies averaged across our study region ($r = -0.05$, $p = 0.69$, 1958–2022), possibly owing to opposing rainfall effects of the SAM in the northern and southern parts of the drought region (*13*). The SAM was mostly neutral throughout the 2017–2019 drought and switched regularly between its positive and negative phases (Fig. 5F). An exception to this was the strong and sustained negative SAM that developed following a Sudden Stratospheric Warming event over Antarctica in the spring of 2019. This event likely exacerbated drying and increased bushfire risk towards the end of the Tinderbox Drought (*13*, *41*).

Moisture sources

Although there is a significant connection between distant climate drivers and SST anomalies to precipitation over the Tinderbox Drought region, the actual sources of moisture for this region are generally more local. The primary source of moisture contributing to southeast Australia's rainfall comes from the Coral and Tasman Seas, immediately to the east of Australia (*20*). Here, we use the Lagrangian model named FLEXPART to understand how moisture sources varied during the drought event (see Methods and (*42*) for further details). The Lagrangian model estimates that on average, 95% of moisture supplied to the Tinderbox Drought region comes from local sources near eastern Australia, extending to the Tasman and Coral Seas ((*20*, *42*), Fig. S7). About 30% (71.4mm) of these moisture sources occur during the cool season from April to September, i.e. the time of the year when rainfall was consistently low during the Tinderbox Drought. Of those cool season moisture sources, 65.7% are from the nearby ocean, while 34.3% come from the land.

Analysis of moisture source regions suggests that the Tinderbox Drought was initiated and sustained by a decline in oceanic moisture supply to the drought region in 2017–2019, and exacerbated in 2018 and 2019 by reduced moisture supply from terrestrial sources. Our analysis indicates that in the 2017 cool season (April–July) the moisture supplied by the oceanic sources was 16% weaker than usual (Fig. 6A, Fig. S8A). The decline in oceanic moisture supply to the region intensified in the cool season of the following year (Fig. 6B), worsening the drought in 2018 (28% lower). In 2019, the oceanic moisture contribution was on average only slightly lower than usual (5% lower). This was characterised by increased oceanic-sourced moisture in the western part of the drought region that partly offset continued negative anomalies from oceanic sources in the eastern part of the Tinderbox Drought region (Fig. 6C). Additionally, the cumulative rainfall deficit over the Tinderbox Drought region also led to anomalously low moisture contribution from terrestrial sources in 2018 and 2019 (Fig. 6E,F; 25% less moisture in 2018, and 27% less in 2019), which exacerbated the severity of the drought.

Interestingly, SSTs in the Coral and Tasman Seas were warmer than usual during much of the Tinderbox Drought, which might have been expected to increase oceanic moisture to the drought region (Fig. S6). Warm SSTs combined with increased wind speed (Fig. 6G-I) and below normal specific humidity (Fig. S8G-I), did indeed promote evaporation (Fig. S8D-F) from the main oceanic source regions. However, anomalous anticyclonic circulation (Fig. 6G-I) transported moisture away from the Tinderbox Drought region toward the northern parts of Australia and the Maritime Continent. This is evidenced by the positive oceanic moisture sink anomalies over Queensland in 2017–18 and extending over the Northern Territory in 2019 (Fig. 6A-C).

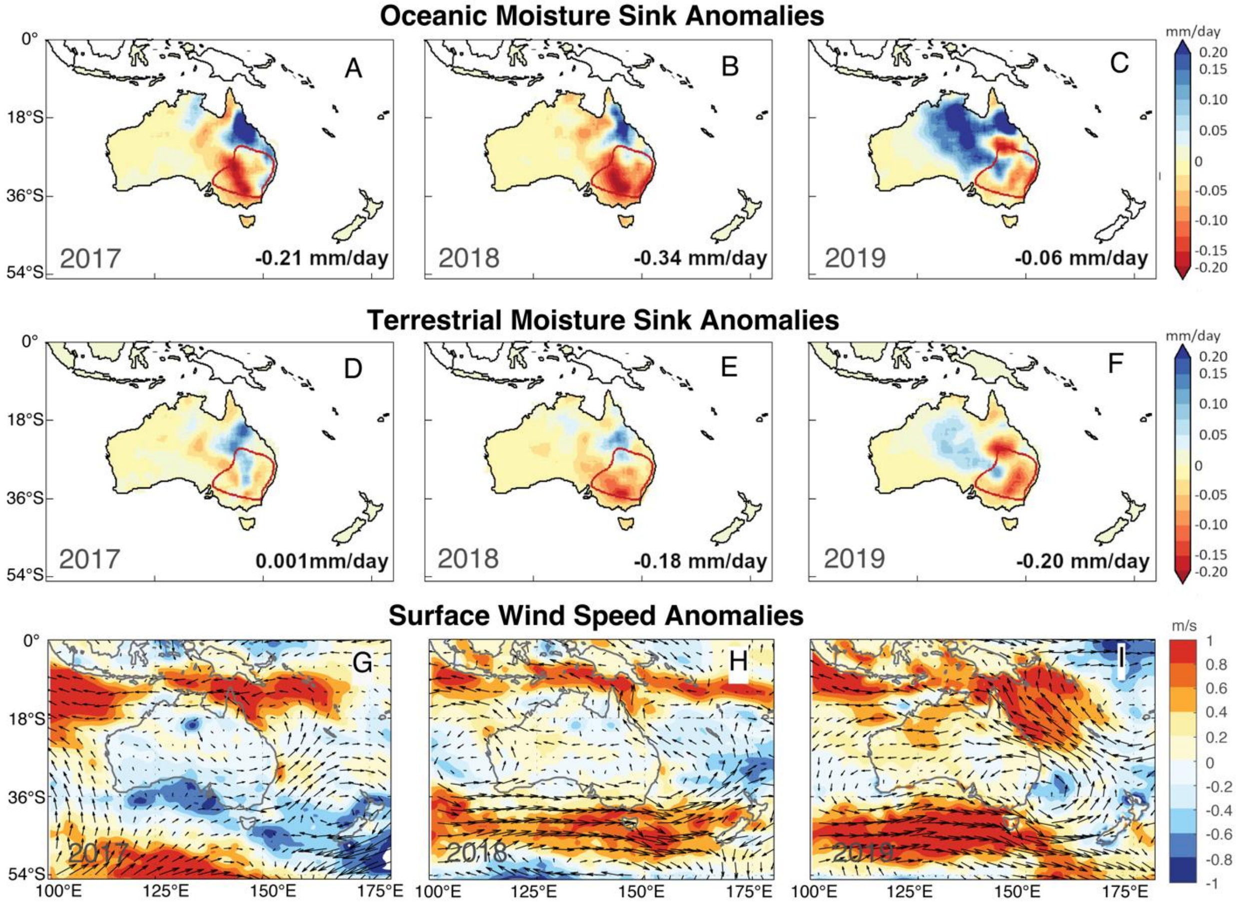

Fig. 6. Sources of moisture during the Tinderbox Drought. Anomalies of (**A,B,C)** oceanic moisture sink (mm/day), (**D,E,F**) terrestrial moisture sink (mm/day), and (**G,H,I**) 850hPa winds (m/s, vectors) and wind speed (m/s, shading). Anomalies are calculated relative to April-to-July 1980-2016 climatology from April to July for (**A,D,G**) 2017 (**B,E,H**) 2018, and (**C,F,I**) 2019 relative to April–July 1980–2016 climatology. Note that the analysis uses a shorter cool season (April to July) due to ERA-Interim data availability (stops in Aug 2019). April–September moisture source and sink anomalies for 2017 and 2018 can be seen in Fig. S9.

Synoptic factors

Reductions in seasonal-scale rainfall during the Tinderbox Drought were partly connected to remote SST anomalies and transport of oceanic-sources moisture, but were ultimately the result of changes to synoptic scale weather systems on daily time scales. Rain-bearing weather systems either reduced in frequency, or they produced less rainfall, during the drought.

Rainfall deficits during past droughts in southeast Australia have, in previous studies, been associated with changes in the frequency of rain-bearing weather systems (*43*, *44*) and the amount of rainfall falling per system (*43*). In particular, the absence of weather systems that bring heavy rainfall, equivalent to around the 95th percentile or higher of daily rainfall amounts, are the dominant cause of rainfall deficits during drought in southeast Australia (*45*). The reduction or absence of heavy rain-bearing weather systems can be influenced by large-scale modes of climate variability, stochastic changes to weather regimes, or combinations of both (*46*, *47*). Concurrently, the frequency and intensity of weather systems that limit rainfall over southeast Australia increase during drought, with an increased occurrence and intensity of synoptic-scale anticyclones (that form the quasi-stationary subtropical ridge) during past multi-year drought periods (*48*).

During the Tinderbox Drought there was a shift toward lower daily rainfall totals across the distribution of daily rainfall data from 2017–2019, compared with 1980–2016 climatology. These distributions were computed using rain days only, which were defined as days above 0.01 mm/day, at each grid point within the drought region (Materials and Methods). However, the nature of rainfall changed as well, with a relatively larger decline in heavy rainfall days (Fig. 7A). The Tinderbox Drought region typically receives half or more of its seasonal rainfall from 'heavy rain days' where the rainfall totals are above the climatological 90th percentile of rain days from 1980–2016. Seasonally, DJF, MAM, JJA and SON receive a median of 63, 59, 51 and 51% respectively of their seasonal rainfall accumulations from these heavy rain days. That is, half or more of the seasonal accumulation occurs on just 10% of the days when it rains.

Despite the overall reduction in rainfall from all rain days during the Tinderbox Drought, the relative contribution from heavy rainfall to the seasonal accumulation decreased significantly more than non-heavy rainfall (i.e., rain days < 90th percentile). The relative contribution of heavy rain days to seasonal totals was lower than normal during all seasons from DJF 2016/17 to DJF 2019/20, with median reductions ranging from –7% to –53% (Fig. 7A). Median changes to non-heavy rain days ranged from –36% to +19%. The largest reductions in heavy rain days were during winter (JJA), when the contribution of heavy rainfall to the seasonal total decreased by 45%, 46% and 49% in 2017, 2018 and 2019 respectively. Given the climatological contribution of heavy rainfall days is 51% for JJA, this shows there were very few, if any, heavy rain days during the Tinderbox Drought winters. Indeed, an analysis at the gridbox scale shows that there were no heavy rain days during some winters in some parts of the domain.

The changes to daily rainfall described above can be associated with different types of synoptic weather systems. Six weather objects (i.e., anticyclones, cyclones, fronts, warm conveyor belts, and potential vorticity streamers and cut-off lows) were examined during the winters (JJA) of the Tinderbox Drought when rainfall reductions were most significant. Daily rainfall data was then attributed to each object (Materials and Methods). Throughout the three winters of the Tinderbox Drought, the intensity and frequency of rainfall decreased for every type of weather object examined here (Fig. 7B–E). The largest declines were mainly associated with warm conveyor belts and potential vorticity (PV) streamers. In the winter of 2017 the total rainfall reduction was due to decreased frequencies of rainfall from each type of weather system, with frequency changes for all objects ranked in the lowest 10 years of the 40 year record (Fig. 7C). Decreases in the intensity of weather-associated rainfall were more important during the winters of 2018 and 2019 (Fig. 7D and 7E). In 2019, the rainfall frequency reductions related to cyclones, warm conveyor belt inflows and ascents were the second lowest in the 40 year record, and fronts the third lowest on record. Similarly, the rainfall intensity reductions related to cyclones, warm conveyor belts and cut-offs were the third or second lowest on record; while the rainfall intensity reductions related to PV streamers were the lowest on record (Fig. 7E).

These results suggest that Rossby wave breaking and warm conveyor belts occurred less often in the winter of 2017, and produced less intense rainfall over the domain in the following two winters. The reduced rainfall associated with warm conveyor belts was likely due to reduced moisture at the inflow level of warm conveyor belts and/or weaker ascending air in warm conveyor belts as a result of weakened upward motion forced by the upper-level wave breaking (*49*). In combination with the results from the analyses of moisture sources, it appears that reduced moisture inflow to warm conveyor belts is likely to have been a significant source of the synoptic-scale rainfall reduction during the Tinderbox Drought.

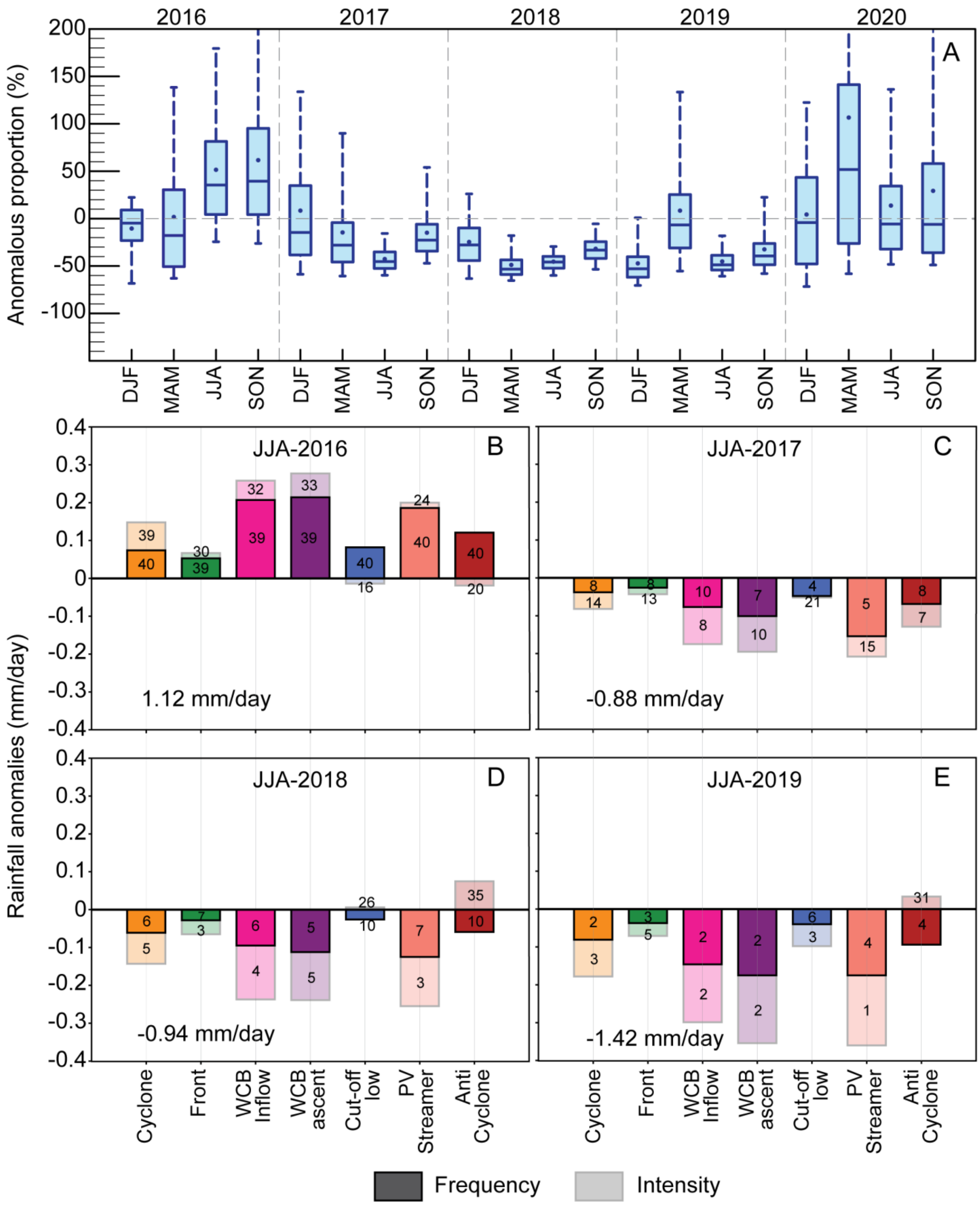

Fig. 7. Rainfall anomalies associated with heavy rainfall days and weather systems during the Tinderbox Drought (**A**) The distribution of the anomalous proportion (%) of seasonal rainfall stemming from heavy rain days from DJF 2015/6 to SON 2020, computed for each grid box in the Tinderbox Drought domain. The anomalous proportion is defined as the proportion of the seasonal rainfall total that falls on days exceeding the climatological 90th percentile of rain days (> 0.01 mm/day). Whiskers show the 5th/95th percentiles, the box the interquartile range, and the median and mean by the horizontal line and dot respectively. For example, if the climatological mean contribution of heavy rain days to a seasonal rainfall total is 70% and during a given year of the drought it was 20%, the value shown is –50%. (**B-E**) The attribution of weather object frequency and intensity change to the daily rainfall anomalies (in mm/day) averaged over the Tinderbox Drought domain are shown for winter (JJA) of (**B**) 2016, (**C**) 2017, (**D**) 2018, and (**E**) 2019. Darker coloured bars represent rainfall changes related to changes in object frequency, and the lighter shading to the intensity of rainfall associated with each object. The numbers within each bar are the rankings of the frequency and intensity anomalies compared to the full 40 years of data from 1980–2019, with 1 the largest negative anomaly and 40 the largest positive anomaly. The daily rainfall anomalies are calculated with respect to all winter days in the period 1980-2016. The numbers indicated in the bottom of panels B-E indicate the area mean rainfall anomaly for each JJA in mm/day equivalent.

Land-atmosphere feedbacks during the drought

Sustained water deficits during droughts can feedback through land-atmosphere coupling to intensify atmospheric heating, and it is notable that the final year of the Tinderbox Drought was Australia's driest and hottest year on record, both in southeast Australia and nationwide (*13*). We examined the impact of soil moisture drought on summer temperatures using the WRF model by contrasting simulations where soil moisture was varied to reflect drought and climatological conditions (Materials and Methods).

The simulated soil water stress experienced by vegetation increased by 10–50% during the Tinderbox Drought relative to climatological conditions across southeast Australia (Fig. S10A and S10F), leading to a decline of 5–60 W m^{-2} in the latent heat flux (Fig. S10B and S10G) and a consequential increase in the sensible heat flux (Fig. S10C and S10H) across widespread areas. As a result, the drier soil moisture increased the summer-mean daily maximum temperature by ~0.25–1.5^{o}C (Fig. S10D and S10I) and decreased air humidity by 2–16 % from the east coast extending to ~400 km inland. During heatwave periods (e.g. 14–26 Jan 2019 and 16 Dec 2019–7 Jan 2020), the soil moisture drought exerted an increasingly strong constraint on transpiration (Fig. S10K and S10P). Overall, the drought conditions and the consequential changes in sensible and latent heat fluxes amplified heatwaves by up to 2.5^{o}C, as well as tended to dry the lower atmosphere. These changes, in turn, are likely to have led to further drying and the elevated fire risk that culminated in the Black Summer fire disaster.

Predictability of the drought

The development of the Tinderbox Drought in mid-2017 occurred during a time when more normal rainfall conditions were expected in southeast Australia (*50*). Neutral states of the ENSO and IOD during 2017 and 2018 meant that indicators that often point to heightened drought risk were absent. Other aspects of the drought, including the development of soil and agricultural drought indicators ahead of meteorological indicators, and the heightened temperature and high VPD conditions in which this drought formed compared with previous droughts, all point to the challenging and changing conditions that may have affected predictability of the Tinderbox Drought.

Machine learning based insights into predictability

Machine learning may offer new insights into the predictability of drought, particularly given the multitude of factors that together resulted in the Tinderbox Drought. Here, we apply the artificial intelligence method used by (*51*) to the Tinderbox Drought. The method combines machine learning based on a Random Forest model and a database of observed drought impacts to explain the contribution of multiple predictors to the drought (see Methods). It performs a "feature importance analysis" that calculates a score that represents the importance of each of the predictors in the model.

Concentrating on 2019 (due to data availability, see Methods), the feature importance analysis indicates that ENSO was not a dominant driver of the drought in 2019 (Fig. 8). This is despite Australian droughts overall being sensitive to large-scale climate drivers, and ENSO in particular, as shown by an analysis of all drought events that have occurred since 2000 (Fig. 8, blue bars). Drought sensitivity in 2019 to other climate modes that are commonly associated with droughts in southeast Australia decreased for the IOD and slightly increased for SAM, yet both offered some predictability of the drought probability in 2019.

In contrast, the local climate, as represented by 3-month precipitation accumulation, soil moisture, evapotranspiration and potential evapotranspiration, provided the most relevant information for predicting drought probability in 2019. For each of these local climate-based predictors, their importance to predictability of the Tinderbox Drought in 2019 was far greater than in other droughts of the past two decades. This may reflect the importance of land-atmosphere processes that intensified the Tinderbox Drought during its final year.

Overall the machine learning method suggests that ENSO did not play a major role in predicting the likelihood of drought in 2019 (confirming our results from the section *Large scale climate drivers*). Instead, local climate features played the largest role in determining drought probability. This suggests that information from both large-scale climate drivers and local climate is necessary for accurate prediction of the conditions associated with the Tinderbox Drought in 2019.

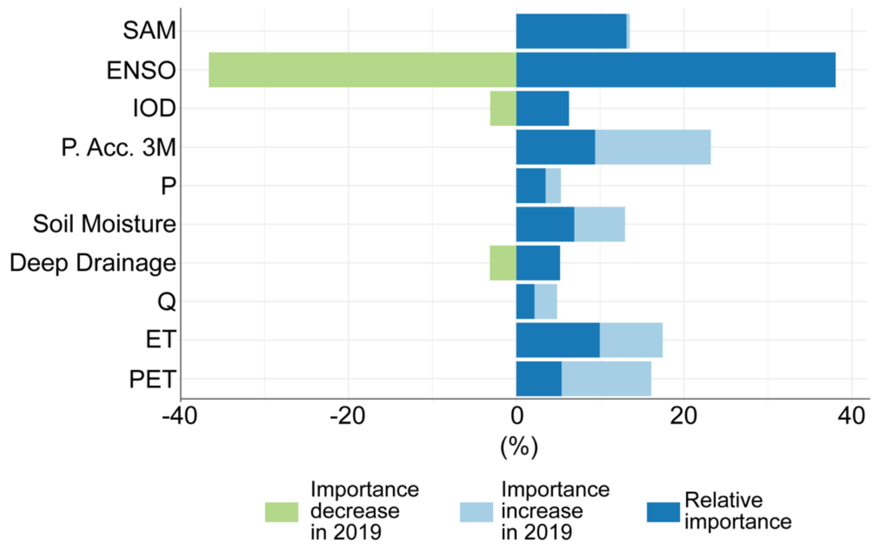

Fig. 8. Feature importance of predictors used in Random Forest model. Predictors include SAM, ENSO, IOD, P.Acc.3M (precipitation accumulated over 3 months), P (precipitation), soil moisture (at root zone), deep drainage, Q (runoff), ET (evapotranspiration) and PET (potential evapotranspiration). Blue bars show the relative importance of the predictors based on all drought events from 2000, green (light blue) bars show the decrease (increase) in relative importance of predictors in the 2019 drought.

Using the same Random Forest approach, we quantified how the probability of drought derived from the local climate and the large-scale modes of variability evolved over time and space during 2016–2020 (Fig. S11). In 2016, the prevailing climate conditions made drought less likely to occur during the winter and spring months (June to November). In contrast, climate conditions during the winters of 2017, 2018 and 2019 indicated a high likelihood (> 0.5 and typically higher than 0.7) of drought. Between February 2019 and February 2020, the probability of drought was very high across the entire region (most months > 0.7), in particular July–August 2019 and October 2019 – February 2020. The multivariate machine-learning approach demonstrates that skillful prediction of the Tinderbox Drought was possible, even in the absence of extreme anomalies in a single predictor of drought.

Probability of drought-breaking

Predicting when droughts are likely to end is also a critical aspect for adaptation responses to multi-year droughts. We examine another aspect of predictability by analysing the influence of large-scale climate drivers on drought breaking rain probabilities during the Tinderbox Drought. This draws on recent advances suggesting that the role of the major modes of variability in inhibiting drought-breaking rain, and thus allowing droughts to develop and continue, may be more important than their role in generating the dry conditions that lead to drought (*35*). Our results show that in 2017 neither ENSO nor IOD contributed substantially to lower the probability of drought breaking rain. In 2018 ENSO contributed to some degree, and in 2019 IOD contributed more strongly to lowering the probability of drought breaking rain (Materials and Methods).

We use a logistic regression method (*52*) to estimate the probability of soil moisture drought breaking within the next 8 weeks during the Tinderbox Drought. The method estimates drought breaking probabilities as a function of time of year, current soil moisture state and ENSO and IOD, and has been shown to perform well in southeastern Australia (*52*). Soil moisture drought is defined based on percentile thresholds that vary by day of year. Fig. S12 shows the area average probability (green line), and the area average probability contributions from the status of the climate modes (light, and dark green shading) in the drought focus region for periods when more than half the grids in the Tinderbox Drought focus region experienced soil moisture drought. The status of the climate modes reduced the probability of drought-breaking in the cool season.

There is a seasonal pattern in soil moisture drought spells in the drought focus region. More than half the grids in the region experienced soil moisture drought from July to October of all three years of the Tinderbox Drought, following the cool season deficits in rainfall (Fig. S12, black line). More than half the grids also experienced soil moisture drought during some months in the warm seasons in 2019 and 2020 (Jan to Mar 2019, Dec 2019 to Jan 2020). In 2017, the probability of drought-breaking was higher than 50% and the states of ENSO and IOD did not contribute substantially to this probability. In the winters of 2018 and 2019, the probability of drought-breaking was lower (around 40%). The main contributor to the lower probabilities of drought-breaking was ENSO in 2018, and IOD in 2019. The state of the climate modes reduced the overall probabilities by 10–15%. The higher influence of IOD in 2019 from this method is consistent with the inference from the machine learning model for impact-based drought metrics (section 5.1). In contrast to the cool season, the probability contributions of the IOD and ENSO were minimal for drought spells during the warm periods in 2019 and 2020, resulting in drought-breaking probabilities that were high (≥60%).

The role of climate change in exacerbating the drought

The severity of the Tinderbox Drought, and the different characteristics of this drought relative to previous droughts in southeast Australia, lead to questions about the extent to which this drought may have been worsened by human-caused climate change. The contribution of anthropogenic forcing to the Tinderbox Drought was estimated following the method described by (*8*) using climate model simulations from the Coupled Model Intercomparison Project phase 6 (CMIP6).

We first estimated how unusual the rainfall anomaly observed during the Tinderbox Drought was in the context of unforced variability in pre-industrial control simulations. Our results show that the observed rainfall deficit during the Tinderbox Drought was unusually large compared to internal (i.e., unforced) model variability; it is estimated that there was only a 0.06% probability of occurrence of such an extreme rainfall deficit arising from modelled internal variability alone (Fig. 9C). This complements our earlier assessments (Fig. 4) that the rainfall deficits were also highly unusual compared to the expected range of internal variability based on historical observations. Such an anomalous rainfall deficit could be explained by the Tinderbox Drought being an exceptionally rare natural event (i.e., very bad luck), or an extreme event that has been exacerbated by anthropogenic forcing of the climate.

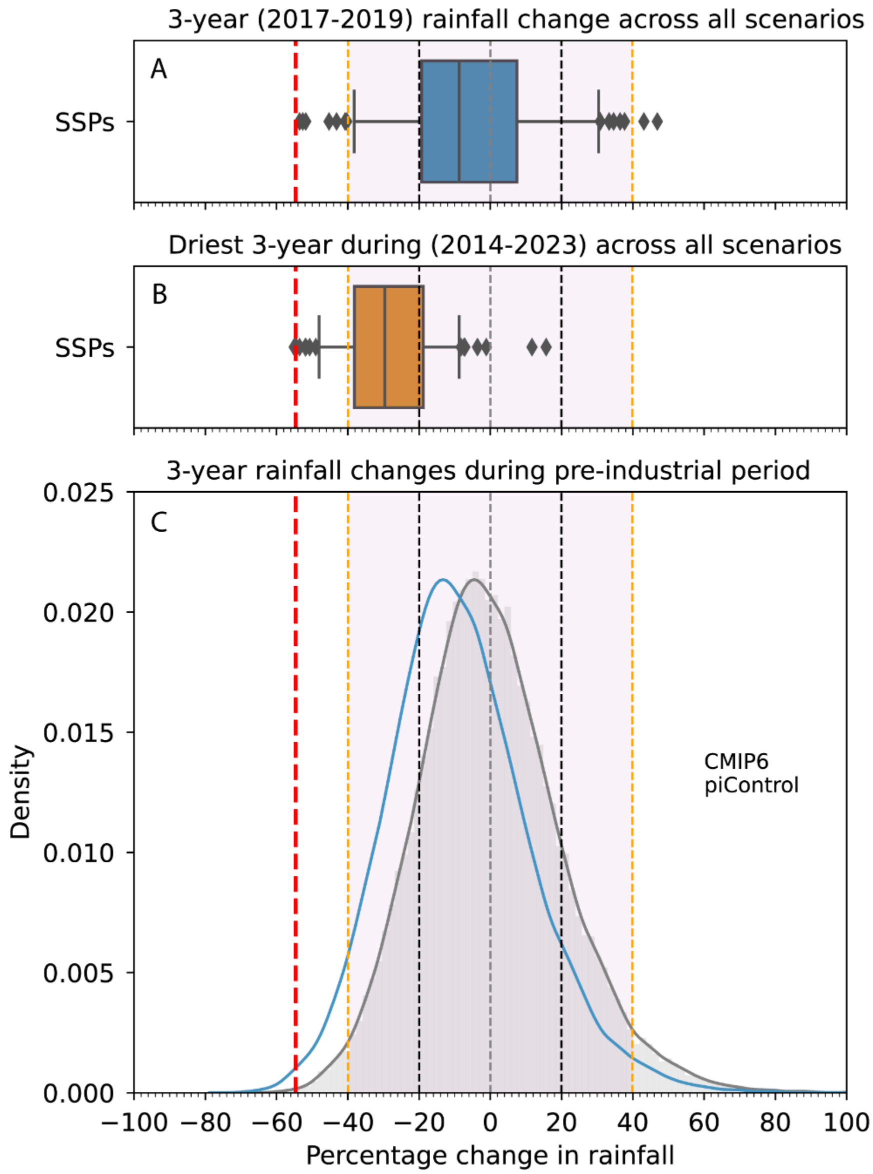

Fig. 9. Contribution of anthropogenic forcing. Percentage changes in area-averaged cool season rainfall of (**A**) the Tinderbox Drought (2017–2019) period, and (**B**) the driest 3-year period between 2014–2023 relative to 1900–1959 period average in CMIP6 models. Box-plots show the spread of change in rainfall based on historical simulations (to 2014) extended to year 2024 with 33 models under SSP5.85, 28 models under SSP3.70 and 31 models under SSP2.45 and SSP1.26 scenarios. We group all SSPs together for this analysis owing to the similarity of forcing in 2017–2019 across all scenarios. The vertical line in the box indicates the median, the box represents the interquartile range and the whiskers indicate the 5th and 95th percentiles. (**C**) The range of a possible 3-year change due to internal variability alone based on CMIP6 models under pre-industrial conditions. One and two standard deviations of the distribution due to internal variability alone are shown as vertical dashed lines in black and orange colours. The blue bell curve is the same as the shaded curve, except that it is shifted left by the median value (i.e., our estimate of the externally-forced response) of the boxplot shown in panel (**A**). The

observed % change is indicated using the thick vertical red dashed line in all panels.

We estimated the contribution from anthropogenic forcing to the rainfall anomaly during the Tinderbox Drought by assessing 2017–2019 cool season rainfall anomalies for the drought region across future climate change scenarios (see Methods). The distribution of 3-year cool season rainfall anomalies simulated for 2017–2019 in the models demonstrates a negative shift relative to the distribution of unforced rainfall anomalies (Fig. 9A). The median percentage contribution of anthropogenic forcing to the observed cool season rainfall deficit during the Tinderbox Drought was 18.4% with an interquartile range of 34.9% to –13.3% across the multimodel ensemble. Assessment of the Millennium Drought in Victoria using the same method produced similar results, suggesting an ~20% anthropogenic contribution to the cool season drying that occurred during that event (*8*). These results are consistent with future climate change assessments suggesting that southeast Australia is likely to experience a long-term decline in cool-season rainfall during the 21st century, but these assessments also currently have low confidence due to the large intermodel spread (*53*).

We do note, however, that even with the incorporation of anthropogenic forcing very few CMIP6 simulations (3 out of 123) simulate 3-year cool season anomalies drier than –50%, and none are able to simulate the full magnitude of the observed deficit in rainfall during 2017–2019 (Fig. 9A). This remains true even if we account for interannual variability by examining the driest 3-year periods simulated by the models during the decade from 2014–2023 (Fig. 9B), rather than specifically 2017–2019 (Fig. 9A). In Fig. 9B, only one simulation is as dry as the observed rainfall deficit during the Tinderbox Drought and six simulations are drier than –50%. This suggests that in addition to anthropogenic intensification of the drought, the natural component of the Tinderbox Drought event was still highly unusual.

Describing the Tinderbox Drought as an extreme natural event that was exacerbated by human-caused climate change is further demonstrated by the results presented in Fig. 9C. The blue bell curve in Fig. 9C is the relative frequency distribution of internal variability, after it has been shifted to the left (i.e. made drier) by the estimated externally-forced response (i.e. 10%, the median value in Fig. 9A). This shifted curve represents the modelled estimate of the relative frequency distribution of possible precipitation anomalies in the Tinderbox Drought region during 2017–2019, arising from both internal variability and external forcing. While the blue curve has a larger tail area below the observed rainfall anomaly than the unshifted bell curve does (grey curve in Fig. 9C), the probability of occurrence of the observed rainfall anomaly remains very small (4.5%). Taking the models at face value therefore suggests that the Tinderbox Drought was dominated by internal variability, but was also made more likely and more intense by external forcing.

Discussion and Implications

Australia's Tinderbox Drought was a very extreme and impactful event. The drought encompassed meteorological, hydrological and ecological/agricultural drought, causing sustained stresses on water resources and large decreases in agricultural yields leading to severe economic and societal impacts. It helped create favourable conditions for the most intense and widespread outbreak of forest fires ever recorded in southeast Australia, earning the name "Tinderbox Drought". Figure 10 summarises the key characteristics, drivers, and impacts of the Tinderbox Drought.

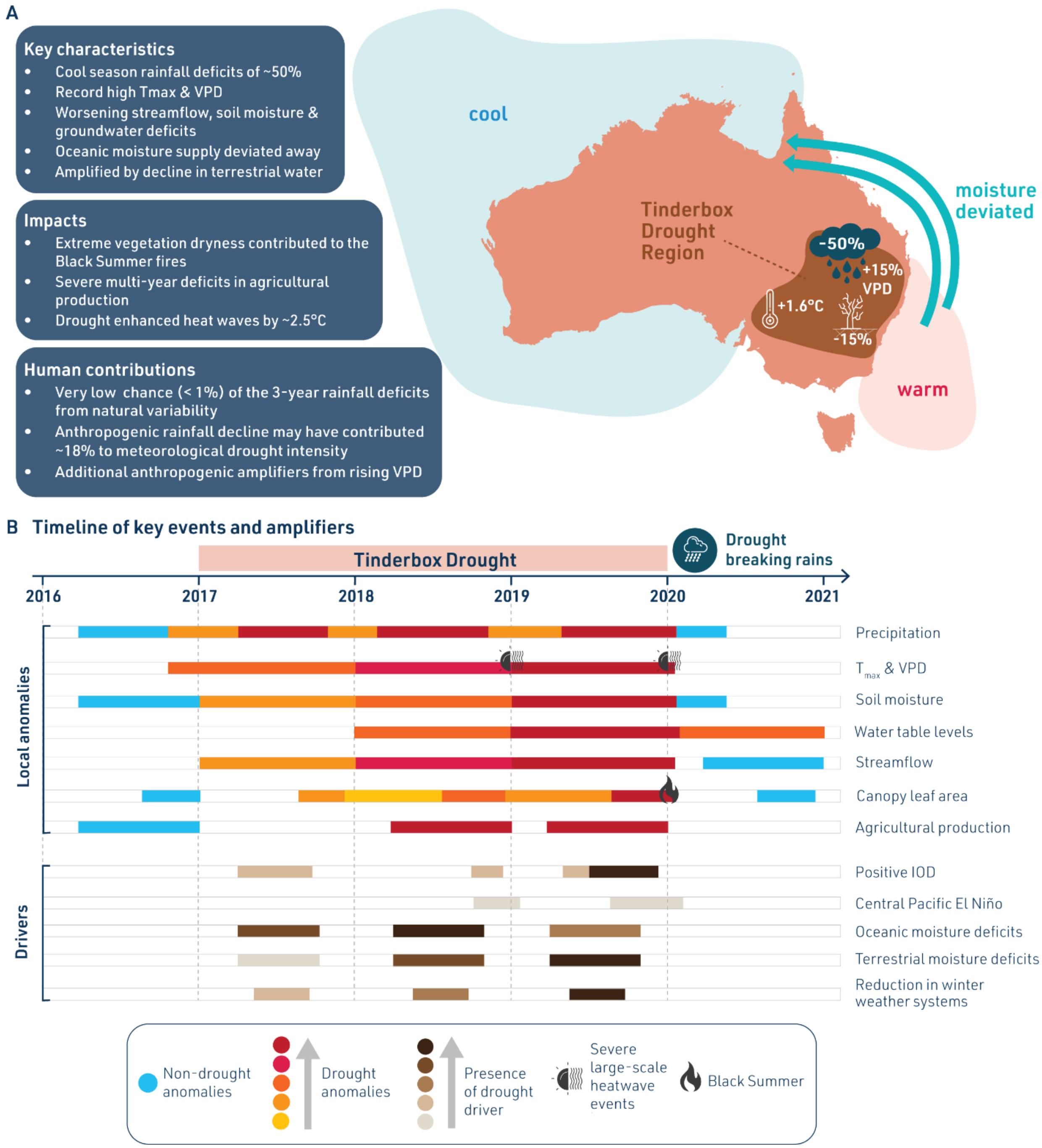

Fig. 10. Characteristics, drivers, and impacts of the Tinderbox Drought. (**A**) Map showing the area most impacted by the drought, highlighting regions of warm and cool SST anomalies likely to have influenced the evolution of the drought. Aqua arrows show the path of moisture deflected away from the drought region, resulting in precipitation deficits. Graphics in the drought area show some of the major characteristics of the drought. (**B**) Timeline of key events and amplifiers of the drought, showing the magnitude of anomalies in relevant metrics (blue and warm colours), and the strength of remote climate drivers (browns). The intensity of shading indicates the strength of the respective drivers and anomalies.

The Tinderbox Drought was sustained and intensified across three consecutive years (2017–2019), characterised by an ~50% decline in cool season rainfall and a 15% decline in surface soil moisture (Fig. 10, Fig. 2). While the rainfall anomalies were most pronounced during the cool season, there were also very few months of positive rainfall anomalies in the intervening warm seasons. As such, sustained declines of evapotranspiration, streamflow, and water storage characterised the intensification of the Tinderbox Drought to its peak in the summer of 2019/20. Temperature and vapour pressure deficit (VPD) were also unusually high during the Tinderbox Drought which amplified the drought impacts on vegetation, with widespread declines observed in vegetation cover during the drought (Figs. 2 and 3). The maximum temperatures during 2017–19 were 1.6°C above the 1980–2016 baseline, and VPD was 15% higher than the 2002–2016 baseline.

Low rainfall, and more specifically the absence of heavy rainfall events, during the Tinderbox Drought was caused by oceanic moisture from the Tasman and Coral Seas being diverted away from southeast Australia and towards northern Australia (Fig. 10, Fig. 6). While sea surface temperature anomalies related to tropical climate variability are known to have strongly influenced past droughts in southeast Australia, ENSO did not play a role in the initiation of dry conditions during the Tinderbox Drought. Rather cool tropical sea surface temperature anomalies to the north and west of Australia, including in the eastern region of the IOD, appear to have been more important in setting up the large-scale conditions that inhibited rainfall over southeast Australia in 2017–2019 (Fig. 5). After being initiated and sustained by remote oceanic conditions, local factors then acted to intensify the Tinderbox Drought and its impacts. Land-atmosphere feedbacks, which result from a strong association of dry and hot conditions in southeast Australia, amplified the intensity of heatwave events in 2018 and 2019 (Fig. 3, Fig. S10). Reduced water availability also resulted in a reduction of local moisture sources over the drought region in 2018 and 2019 (Fig. 6). Drought-breaking rainfall in February of 2020 ended the Tinderbox Drought, though some elements of the hydrological cycle still had not recovered to pre-drought levels almost a year after the meteorological drought broke (Fig. 2).

Climate variability in southeast Australia is high, and the region is renowned for its large swings between “drought and flooding rains”, but evidence points to the Tinderbox Drought being more than just very bad luck. The Tinderbox Drought was exceptionally rare in its severity – in terms of both the 3-year mean rainfall deficit and in the occurrence of three consecutive dry years, and against assessments of internal variability in observational data (Fig. 4) and climate simulations (Fig. 9). Southeast Australia is expected to undergo sustained declines in cool season rainfall as climate change continues this century (*1*, *53*, *54*), and human-caused drying may have already intensified the cool season rainfall deficits of the Tinderbox Drought by around 18% (Fig. 9). However, the Interquartile Range (34.9% to –13.3%) highlights the considerable uncertainty in this estimate, resulting from the inability of current climate simulations to accurately capture rainfall processes in our study region. This includes considerable intermodel spread in projected mean rainfall changes due to human-caused climate change, and limitations in model representations of multi-year drought due to a lack of persistence of simulated rainfall deficits (*2*) and systematic errors in land surface models (*54*).

However, there are also multiple other ways in which human-caused climate change may have worsened the Tinderbox Drought. Elevated temperatures over southeast Australia during 2017-2019 can be unequivocally linked to anthropogenic forcing (*1*, *55*), although the intensity of heatwaves later in this event were also amplified by the drought. The impacts of rising atmospheric temperature on increasing VPD provides a high-confidence mechanism for anthropogenic forcing to increase drought (and fire) risk (*26*) beyond the more direct climate change impacts on rainfall although the degree to which increasing VPD enhances these risks is poorly understood. Drought also feeds back to amplify VPD anomalies, and it is evident that land-atmosphere processes influenced the intensification of the Tinderbox Drought. Nevertheless, record high VPD may have led to local intensification of the impacts of the Tinderbox Drought, something that sets this drought apart from historical conditions in southeast Australia (Fig. 3A). Drought monitoring also showed indicators of hydrological and agricultural drought emerging ahead of meteorological drought indicators. It is possible that this reflects the additional stress on these systems by elevated background temperature and VPD. It is also possible that the hydrological system in southeast Australia was already under stress from the multi-decade dry phase that preceded the Tinderbox Drought, including incomplete recovery from the multi-year Millennium Drought. Anthropogenic climate change is also thought to be altering the way tropical climate variability operates. Trends towards more frequent central-Pacific type El Niño events, and stronger and more frequent positive IOD events, are seen in paleoclimate and observational data (*13*), and these trends are projected to continue in the future as a consequence of human-caused climate change. Both of these large-scale drivers appear to have played some role in remote forcing of the Tinderbox Drought, particularly during 2019 (Fig. 5), and thus may have incorporated a further anthropogenic component that exacerbated the natural variability element of the Tinderbox Drought.

Some aspects of the Tinderbox Drought were unexpected. Our study shows that the traditional indices used to represent the tropical modes of variability may not be optimal for guiding the communication of seasonal outlooks of drought risk in southeast Australia. ENSO, as represented by the Niño3.4 index, provided far less predictive skill of the unfolding rainfall anomalies during the Tinderbox Drought than during previous drought events (Fig. 8). The eastern pole of the IOD appears more important as a predictor than the full DMI, while tropical sea surface temperatures to the north of Australia appear to have more skill in determining cool season rainfall anomalies over our study region than any of the traditional climate mode indicators (Fig. 5). However, our study also highlights the importance of local climate factors in drought intensification and predictability. Furthermore, there are promising pathways forward for the skillful prediction of drought risk when multiple predictors are used simultaneously through machine learning approaches (Fig. 8). This is particularly important as the Tinderbox Drought demonstrates that extreme and impactful droughts are able to develop without any particular indicator of drought risk being in an extreme state.

The Tinderbox Drought illustrates the necessity for multidisciplinary approaches in improving our understanding of the causes, impacts and predictability of multi-year droughts. What is considered a single event can be associated with multiple interacting drivers and impacts that evolve during the event. Past research has tended to focus on understanding droughts and other climate extremes by a single explanation. This study demonstrates how drawing together a diversity of research expertise, and employing powerful new research tools including machine learning, can greatly advance our understanding of complex events. Extending this approach to other droughts in southeast

Australia, and to multi-year droughts in other regions of the world, provides avenues to advance our understanding of past droughts and future drought risk.

Our study has described multiple ways that human-caused climate change may have worsened the Tinderbox Drought. Future projections of climate change indicate that in many regions of the world, including parts of our study region, climate change is expected to make droughts more frequent and more severe (*56*). However, there are serious limitations in the ability of current climate models to simulate multi-year droughts such as the Tinderbox Drought that hinders our understanding of the nature and drivers of Australian droughts. It is also evident that the observational record is not sufficient to capture the full range of possible natural variability in multi-year droughts. Continued quantification of the processes that interact to initiate, sustain and end multi-year droughts, and improved representation of these processes in models, will be required to improve projections of future drought risk and support adaptation decisions. Although not quantified in our study, increasing human demand on water resources also represents a potential further anthropogenic component to the Tinderbox Drought. Changes in human demand for water are not readily incorporated into future projections of drought, but water management practices will be key to managing the risks of future multi-year droughts in southeast Australia and other drought-prone regions.

Materials and Methods

Data

The datasets used for analyses are listed in Table S1.

Drought metrics

We used standardised metrics and percentile thresholds to identify areas that experienced meteorological and agricultural/ecological drought during the years 2017 to 2019. Metrics based on precipitation, potential evapotranspiration (PET), and soil moisture from the multiple datasets listed in Table S1 are used to calculate the drought metrics.

Deficits in precipitation are assessed using the 3-month Standardised Precipitation Index (SPI-3) values less than -1. The -1 threshold corresponds to moderate dryness (*57*). SPI-3 calculated from three precipitation datasets (AGCD, MSWEPv2.8 and CHIRPS-2.0). The Australian Gridded Climate Data (AGCD) is a gauge-based product providing monthly and daily precipitation, temperature, and vapour pressure data at 0.05° x 0.05° spatial resolution (*58*). Multi-Source Weighted-Ensemble Precipitation (MSWEPv2.8) is a global gridded precipitation product that merges gauge, satellite, and reanalysis data at a spatial resolution of 0.1°. Climate Hazards Group InfraRed Precipitation with Station data (CHIRPS-2.0) is another merged product that incorporates satellite imagery and station data to create gridded precipitation data at 0.05° resolution between 50°N-50°S.

The 3-month Standardised Precipitation Evapotranspiration Index (SPEI-3) (*59*), which includes the additional water balance component of PET, is used to identify areas in agricultural/ecological droughts using the same threshold of -1 from two sets of datasets. The Global Land Evaporation Amsterdam Model (GLEAMv3.5) provides estimates of actual and potential evapotranspiration (AET and PET) globally at a spatial resolution of 0.25°. Historical estimates of AET and PET are provided from the Australian Water Resources Assessment Landscape (AWRA-L) model (*60*) at a spatial resolution of 0.05°.

SPEI-3 is calculated using two sets of datasets (1) precipitation from the AGCD and PET from AWRA-L, and (2) precipitation from MSWEPv2.8 and PET from GLEAMv3.5. We also assess seasonal and annual precipitation accumulations and soil moisture below the corresponding 15th percentile thresholds, which broadly corresponds to an SPI/SPEI of -1 and is chosen for consistency. All baseline calculations for SPEI-3, SPEI-3 and the 15th percentile are for 1980 to 2016.

Calculation of hydrometerological anomalies

We use gridded precipitation and actual evapotranspiration from multiple datasets to estimate monthly and seasonal anomalies. We calculate the average precipitation anomalies from AGCD, MSWEPv2.8, and CHIRPS-2.0 datasets. We calculate average evapotranspiration anomalies using estimates from AWRA-L and GLEAMv3.5. We also calculate maximum temperature anomalies from the AGCD dataset. Soil moisture from the European Space Agency Climate Change Initiative (ESACCI) dataset is used to quantify anomalies in surface soil moisture. Monthly and seasonal anomalies in all variables are computed with respect to a baseline period of 1980 to 2016 for datasets except CHIRPS-2.0. A baseline of 1981 to 2016 is used for the CHIPRS-2.0 due to data availability constraints.

We also use shorter records from satellite datasets and field measurements to study changes in other water cycle variables during the drought. Total terrestrial water storage (TWS) anomalies from the Gravity Recovery and Climate Experiment (GRACE) are used to study changes in deeper soil storages. Combined data from the GRACE and GRACE follow-on missions are available for the period 2002 to 2021 and we estimate monthly TWS anomalies with respect to a shorter baseline of 2002 to 2016. Due to the time lag between the two GRACE missions, TWS data during a year of the drought (mid 2017-18) is missing from this dataset. Point measurements of streamflow and water levels in bore wells are available at some locations in the region of interest. Streamflow data at high quality hydrologic reference stations (HRS) are available from BoM, and the length of the record varies by station. Here we study anomalies in streamflow at stations that receive inflows from catchment areas larger than ~1000 km^2 (Fig. 1). We use borewell observations from the Australian groundwater explorer (*61*) to study changes in water table depth, after removing the measurements flagged as low quality. Borewell water level measurements that cover the region and period of interest are generally scarce, but some spatial clusters of data are available primarily for a shorter period from 2010 to 2021 (Fig. 1). A cluster of wells located near the Darling basin region contains measurements for more than 80% of the time during the period 1996 to 2021. The monthly anomalies from climatology in the depth to the water table in these borewells are quantified with respect to a baseline of 1996 to 2016. Further, some clusters of borewells in Darling, Murrumbidgee & Upper Murray, Hunter & Namoi, Lachlan, Gwydir, and Condamine basin regions contain data that cover more than 80% of the period from 2010 to 2021. Hence, we estimate the monthly water level anomalies in these regions with respect to a shorter baseline of 2010 to 2016.

Calculation of vegetation related anomalies

Vegetation anomalies were calculated with respect to 2002-2016, owing to data availability constraints from the satellite datasets. We calculated anomalies on remote sensing derived data, and vapour pressure deficit from the AGCD dataset using data from the satellite derived estimates of Vegetation Optical Depth (VOD) using the LPDR v3 product, which broadly corresponds with canopy water content; the Normalised Difference Vegetation Index (NDVI) from MYD13A2 collection 6.1, which is a well known proxy of canopy area and vegetation productivity; and land skin temperatures from the MYD11A1 collection 6.1 product, which can serve to indicate departures in canopy latent heat flux due to changes in canopy transpiration. VOD and NDVI anomalies during spring (SON) were, on average, the most severe during the drought.

We obtained agricultural statistics from two datasets (listed in Table S1) to assess the impact of the Tinderbox Drought on these crops. We use wheat and barley statistics from the ABARES farm survey data reported for sub-regions within the drought focus region to estimate regional anomalies (https://www.agriculture.gov.au/abares/data/farm-data-portal). In the case of rice and cotton, sub-national statistics are not available. However, as most of the rice and cotton produced in Australia are grown in the Murray Darling Basin (*5*), we use national statistics from the FAOSTAT database (https://www.fao.org/faostat/en/#data/QCL) to assess the impact on these crops. The agricultural datasets are used to estimate the growing season anomalies in area harvested, crop yield, and agricultural production of these crops with respect to a baseline of 1990 to 2016. We use a shorter baseline due to data availability constraints in the ABARES farm survey dataset.

Linear Inverse Modelling

Multi-year seasonal precipitation deficits that contribute to droughts may occur due to natural variability, or require anthropogenic forcings. Determination of whether a particular drought is anomalous (and hence potentially anthropogenically forced) requires a long 'baseline' against which to compare that event. We can estimate the long-term background (unforced) precipitation variability in climate models via long (hundreds of years) simulations with unchanging external forcings. However, we do not know how accurately climate models simulate long-term Australian precipitation variability, particularly in terms of extremes. The observational record of precipitation in south-eastern Australia is not long enough to quantify the full natural range of precipitation variability, particularly in terms of the statistics of multi-year events (*29*, *62*).

Here we use a novel approach which allows estimation of the full distribution of south-eastern Australian precipitation variability, based on the spatial and temporal covariance structure of the observed climate system (assuming stationarity of these structures). Specifically, we assessed whether the 2017-2019 drought was unusual relative to a stochastically-forced system with stationary statistics. We used linear inverse models (LIMs) to calculate an ensemble of precipitation trajectories that maintain the spatial and temporal correlation structure of the observational record. Our approach, based on (*63*) and (*64*), uses a LIM of the form

$$\frac{dX}{dt} = \boldsymbol{LX} + \zeta$$

where **X** is a state vector, **L** is a deterministic feedback matrix describing spatial and temporal autocorrelations, and ζ is a white noise term where data may be correlated in space but not time. To form **X**, we used linearly detrended monthly global SST anomalies, and linearly detrended monthly precipitation amount anomalies over Australia. Inherent in this detrending step is the assumption that long-term trends have an anthropogenic component. We excluded the tropics due to the highly non-linear precipitation. SST data were from two sources: the NOAA Extended Reconstructed SST V5 (ERSST), and the Centennial In Situ Observation-Based Estimates (COBE) listed in Table S1. ERSST is available on an approximately 2° x 2° grid, spanning 1854 to present. COBE is available on a 1° x 1° grid, spanning 1891 to present. Both products are derived from observations from the International Comprehensive Ocean-Atmosphere Data Set. Precipitation data were from the AGCD. In both cases, we applied a three-month running mean prior to construction of the LIMs, and clipped the SST data to 60°S-60°N. As in (*64*), the precipitation portion of **X** was heavily down-weighted such that SST impacts precipitation in **L**, but precipitation does not impact SST. We ran each LIM version (one with SST from ERSST and one with SST from COBE) 100 times, for 117 years, resulting in 11700 years of simulated three-month-smoothed monthly precipitation variability driven by each SST product.

We used our LIM-derived estimate of long-term natural variability to calculate the probability of experiencing one, two, and three sequential years with precipitation deficits equal to or greater than the least severe deficit of the three years of the drought. For the annual-mean and AMJJAS, this was 2017. For DJF, this was 2018. This forms a null hypothesis against which to test the proposition that this drought occurred within the expected range of long-term natural variability.

Moisture tracking model

Southeast Australia's rainfall is affected by moisture supply from nearby oceans (*20*) and influenced by remote climate drives such as ENSO and IOD. Apart from the strong 2019 IOD that coincided with the late stages of the drought, the remote climate drivers could not fully explain the onset and development of the drought (*12*). Here we look into local processes and explore the role of moisture sources and transport to the region as alternative mechanisms for understanding the genesis and evolution of the Tinderbox Drought.

We use the Lagrangian FLEXible PARTicle (FLEXPART) dispersion model (*65*) to track water vapour in the atmosphere and identify the sources and sinks of moisture during the drought event. In this model the global atmosphere is divided into approximately 2 million finite elements, called "particles", with constant mass transported using 3D wind fields. The model calculates changes in freshwater flux (evaporation, e, minus precipitation, p) associated with each particle for every time step, i.e. $e - p = m(\mathrm{d}q/\mathrm{d}t)$, where q is the specific humidity of each particle and m is the mass of the particle. The total (E − P) surface freshwater flux is then calculated by adding (e − p) for all the particles residing in the atmospheric column over a given area. Details of the model can be found in (*65*).

We use ERA-Interim Reanalysis to provide the 6-hourly data for winds and humidity at 61 atmospheric levels at 1^{o} x1^{o} degree resolution. FLEXPART has been shown to provide a satisfactory representation of the hydrological cycle (*66*).

The Lagrangian model is integrated backward in time to identify the sources regions that supply moisture for the precipitation over the region. The model is then integrated forward in time from the identified moisture sources to obtain the individual contribution from ocean and land to precipitation. The integration time is equivalent to the residence time of water vapour in the atmosphere and varies according to regions and seasons (*67*). For Australia, the optimum integration time is 6-10 days ((*68*); Table S2).

Weather feature analysis

Weather feature datasets are used to investigate the behaviour of weather systems over Australia to identify anomalous weather patterns during the drought. The datasets are established based on objective identification of weather or flow phenomena, and they allow analysing the occurrence frequency, spatial distribution and temporal variability of a specific weather system (*69*). All weather or flow features are identified as hourly two-dimensional binary fields, with the value 1 representing the occurrence of the weather system at grid points and the value 0 indicating no weather system identified. A meaningful set of weather or flow phenomena that affect rainfall over the region of interest (Fig. 1) are selected in the analysis, including extratropical cyclones, fronts, and anticyclones (e.g., (*70*, *71*)). In addition, warm conveyor belts, potential vorticity streamers and cut-offs (indicating the Rossby wave breaking near the extratropical tropopause) are considered. Warm conveyor belts are the major precipitating part of extratropical cyclones (*72*), and potential vorticity streamers and cut-offs act as a precursor for heavy rainfall events (e.g.,(*73*)). The identification algorithms of cyclones, anticyclones, warm conveyor belts, and potential vorticity streamers and cut-offs are detailed in (*69*).

Whether the changes in rainfall are due to changes in the frequency and intensity of the rainfall from a particular weather system is investigated in a similar way to (*74*). We note that the rainfall attributed to each weather object does not sum to the total rainfall for that season for two reasons. The first is that rainfall is not exclusively attributed to an object, as weather objects can overlap with each other, reflecting the nature of co-occurrence of weather systems, such as PV streamers and cut-off lows. As a result, the relative contribution of overlapped weather objects to rainfall cannot be quantified. Second, it could be that no object described here was in the vicinity when rainfall was recorded, since there are likely to be other rainfall-producing processes not captured by the six weather objects. However, the vast majority of rainfall is accounted for by the weather objects examined.

Land-atmosphere model simulations

To analyse the impact of drought on summer temperatures and heatwave extremes we implement the WRF-LIS-CABLE modelling system, which includes the Community Atmosphere Biosphere Land Exchange (CABLE) land surface model (LSM) and the National Aeronautics and Space Administration (NASA) Unified Weather Research and Forecasting (NU-WRF) model version 9.2. The version of CABLE LSM includes an explicit groundwater aquifer and has been evaluated at scales ranging from a site to global scales (*75*). To obtain the equilibrated initial land states, we force the standalone CABLE LSM using the resampled 3-hourly AGCD dataset (*58*) for 90 years with fixed CO_2 concentrations, and then for the period 1970-2019 with varying CO_2 concentrations (see (*76*)).

We use the WRF atmospheric physics configurations suggested by (*77*) for southeast Australia. This includes the WRF Single-Moment 5-class microphysics scheme, the Mellor-Yamada-Janjic boundary layer and surface layer schemes, as well as the New Goddard shortwave and longwave radiation schemes. The simulations of the 2017-2019 drought (hereafter DROUGHT) are initialised using the equilibrated land conditions from the offline simulation on 30 Nov 2018 and on 30 Nov 2019, separately, and then run through the 2018/2019 and 2019/2020 summers forced by the ECMWF Reanalysis v5 (ERA5) dataset at 4 km resolution over southeast Australia. We also run a simulation with climatological soil moisture by using the 1970-1999 averaged soil and aquifer moisture on 30 Nov 2018 and 2019 (hereafter CLIM).

Impact based drought indicators using machine learning

To complement the analyses of local hydrological variables and the large-scale modes of variability, we also examined what these climate features and their interactions can collectively tell us about the temporal and spatial development of this drought. To achieve this, we analyse written drought impact reports, noting the time, location of ‘drought’ and ‘no drought’ events, coincident conditions and values of large-scale climate indicators. Then, using machine learning, we establish a predictive model of drought impact, based on climate conditions and large scale climate modes as predictors.

We follow (*51*), but develop an equivalent database of drought events for the region of interest in Australia. Monthly drought impacts reported by the Bureau of Meteorology (BoM), the NSW Department of Primary Industries (DPI) and NSW Department of Planning, Industry & Environment (DPIE) were used. Several local drought-related variables (precipitation, 3-month precipitation accumulation, soil moisture, evapotranspiration, potential evapotranspiration, deep drainage, and runoff) were used together with large scale modes of climate variability at monthly time steps as predictors for these events, simply labelled as binary ‘drought’ or ‘no drought’ events. In total, 935 labelled samples are used to train and validate a ML drought indicator, with the number of samples varying by year. Table S1 lists the data sources of the predictors.

The relationship was derived using a Random Forest (RF) classifier (*78*) at a monthly timescale. The trained Random Forest model, which we referred to as the ‘RF-drought indicator’ was then used to calculate the probability of drought over the region of interest for 2016 to 2021. This allows us to build a non-linear multivariate drought index that can predict the conditional probability of drought and also provide information about which predictors have the most predictive power in discerning ‘drought’ and ‘no drought’ events. The performance of the RF-drought indicator is tested using data not used for training. Using the RF model, we additionally perform a feature importance analysis to quantify the importance of each predictor in the model. We use this analysis to identify the drivers of the 2019 drought conditions, concentrating on this year due to a higher number of available samples from the impact reports.

Soil moisture drought-breaking probabilities

We apply the logistic regression method documented in (*52*) to estimate the probability of ongoing soil moisture drought events ending within the next 8-weeks. We use the results to assess the contributions of the climate modes to drought breaking probabilities. We briefly summarise the method below and direct the reader to the original paper for more detail.

Soil moisture drought spells are identified using root zone soil moisture from the AWRA-L model historical dataset based on percentile thresholds calculated separately for each day of the year. A drought spell starts when the soil moisture falls below the 10^{th} percentile and ends when it increases above the 30^{th} percentile. The soil moisture change required to end an ongoing drought event is calculated as the amount of moisture change required to exceed the 30^{th} percentile. Historical data is then used to estimate the probability of exceedance of the requisite soil moisture changes (i.e., the drought-breaking probability) as a function of the states of the climate modes. We use historical data from

1911 to 2016 to train the logistic regression models and estimate drought breaking probabilities within 8 weeks. We also use the results to study the evolution of the contributions of ENSO and IOD to the drought breaking probabilities.

Estimating the role of climate change

We used monthly precipitation for the first ensemble member (i.e., r1i1p1f1) of the preindustrial and historical experiment and four different future emissions scenarios (see Table S3 for the list of models used). The magnitude of the anthropogenic-forced drying in the 2017-2019 period in models is estimated by averaging the multi-model median (MMM) values across four emission scenarios, weighted by the number of models used under that scenario (see (*79*)). Finally, the anthropogenically-forced component is estimated by determining the proportional contribution of the averaged-MMM value to the observed change. The Interquartile Range of the individual model estimates are also provided.

References

1. IPCC, "Summary for Policymakers" in Climate Change 2021: The Physical Science Basis. Contribution of Working Group I to the Sixth Assessment Report of the Intergovernmental Panel on Climate Change [Masson-Delmotte, V., P. Zhai, A. Pirani, S.L. Connors, C. Péan, S. Berger, N. Caud, Y. Chen, L. Goldfarb, M.I. Gomis, M. Huang, K. Leitzell, E. Lonnoy, J.B.R. Matthews, T.K. Maycock, T. Waterfield, O. Yelekçi, R. Yu, and B. Zhou (eds.)], V. Masson-Delmotte, P. Zhai, A. Pirani, S. L. Connors, C. Péan, S. Berger, N. Caud, Y. Chen, L. Goldfarb, M. I. Gomis, M. Huang, K. Leitzell, K. Lonnoy, J. B. R. Matthews, T. K. Maycock, T. Waterfield, O. Yelekçi, R. Yu, B. Zhou, Eds. (Cambridge University Press, Cambridge, United Kingdom and New York, NY, USA, 2021; 10.1017/9781009157896.001), pp. 3–32.

2. S. I. Seneviratne, X. Zhang, M. Adnan, W. Badi, C. Dereczynski, A. D. Luca, S. Ghosh, I. Iskandar, J. Kossin, \ S. Lewis, F. Otto, I. Pinto, M. Satoh, S. M. Vicente-Serrano, M. Wehner, B. Zhou, "Weather and Climate Extreme Events in a Changing Climate" in Climate Change 2021: The Physical Science Basis. Contribution of Working Group I to the Sixth Assessment Report of the Intergovernmental Panel on Climate Change [Masson-Delmotte, V., P. Zhai, A. Pirani, S.L. Connors, C. Péan, S. Berger, N. Caud, Y. Chen, L. Goldfarb, M.I. Gomis, M. Huang, K. Leitzell, E. Lonnoy, J.B.R. Matthews, T.K. Maycock, T. Waterfield, O. Yelekçi, R. Yu, and B. Zhou (eds.)], V. Masson-Delmotte, P. Zhai, A. Pirani, S. L. Connors, C. Péan, S. Berger, N. Caud, Y. Chen, L. Goldfarb, M. I. Gomis, M. Huang, K. Leitzell, E. Lonnoy, J. B. R. Matthews, T. K. Maycock, T. Waterfield, O. Yelekçi, R. Yu, B. Zhou, Eds. (Cambridge University Press, Cambridge, United Kingdom and New York, NY, USA, 2021; 10.1017/9781009157896.013), pp. 1513–1766.

3. X. Yuan, Y. Wang, P. Ji, P. Wu, J. Sheffield, J. A. Otkin, A global transition to flash droughts under climate change. Science. **380**, 187–191 (2023).

4. B. Edwards, M. Gray, B. Hunter, The social and economic impacts of drought. Australian Journal of Social Issues. **54**, 22–31 (2019).

5. A. I. J. M. Van Dijk, H. E. Beck, R. S. Crosbie, R. A. M. De Jeu, Y. Y. Liu, G. M. Podger, B. Timbal, N. R. Viney, The Millennium Drought in southeast Australia (2001-2009): Natural and human causes and implications for water resources, ecosystems, economy, and society. Water Resources Research. **49**, 1040–1057 (2013).

6. Z. Hao, V. P. Singh, Y. Xia, Seasonal Drought Prediction: Advances, Challenges, and Future Prospects. Reviews of Geophysics. **56**, 108–141 (2018).

7. A. S. Kiem, F. Johnson, S. Westra, A. van Dijk, J. P. Evans, A. O'Donnell, A. Rouillard, C. Barr, J. Tyler, M. Thyer, D. Jakob, F. Woldemeskel, B. Sivakumar, R. Mehrotra, Natural hazards in Australia: droughts. Climatic Change. **139**, 37–54 (2016).

8. S. P. Rauniyar, S. B. Power, The Impact of Anthropogenic Forcing and Natural Processes on Past, Present, and Future Rainfall over Victoria, Australia. Journal of Climate. **33**, 8087–8106 (2020).

9. D. G. C. Kirono, V. Round, C. Heady, F. H. S. Chiew, S. Osbrough, Drought projections for Australia: Updated results and analysis of model simulations. Weather and Climate Extremes. **30**, 100280 (2020).

10. J. Lu, G. J. Carbone, J. M. Grego, Uncertainty and hotspots in 21st century projections of agricultural drought from CMIP5 models. Scientific Reports. **9**, 4922 (2019).

11. BoM, “Special Climate Statement 70 update—drought conditions in Australia and impact on water resources in the Murray–Darling Basin” (2019), (available at http://www.bom.gov.au/climate/current/statements/scs70b.pdf).

12. H. Nguyen, M. C. Wheeler, H. H. Hendon, E.-P. Lim, J. A. Otkin, The 2019 flash droughts in subtropical eastern Australia and their association with large-scale climate drivers. Weather and Climate Extremes. **32**, 100321 (2021).

13. N. J. Abram, B. J. Henley, A. Sen Gupta, T. J. R. Lippmann, H. Clarke, A. J. Dowdy, J. J. Sharples, R. H. Nolan, T. Zhang, M. J. Wooster, J. B. Wurtzel, K. J. Meissner, A. J. Pitman, A. M. Ukkola, B. P. Murphy, N. J. Tapper, M. M. Boer, Connections of climate change and variability to large and extreme forest fires in southeast Australia. Communications Earth & Environment. **2**, 8 (2021).

14. J. Lawrence, B. Mackey, F. Chiew, M. J. Costello, K. Hennessy, N. Lansbury, U. B. Nidumolu, G. Pecl, L. Rickards, N. Tapper, A. Woodward, A. Wreford, "Australasia" in Climate Change 2022: Impacts, Adaptation, and Vulnerability.Contribution of Working Group II to the Sixth Assessment Report of the Intergovernmental Panel on Climate Change [H.-O. Pörtner, D.C. Roberts, M. Tignor, E.S. Poloczanska, K. Mintenbeck, A. Alegría, M. Craig, S. Langsdorf, S. Löschke, V. Möller, A. Okem, B. Rama (eds.)] (Cambridge University Press, Cambridge, UK and New York, NY, USA, 2022; 10.1017/9781009325844.013), pp. 1581–1688.

15. NSW DPI, “NSW State Seasonal Update - December 2019” (ISSN 2202-1795 (Online). Volume 7 Issue 12., 2020), (available at https://www.dpi.nsw.gov.au/climate-landing/ssu/december-2019).

16. S. Hatfield-Dodds, N. Hughes, A. Cameron, M. Miller, T. Jackson, “Analysis of 2018 drought: 26 October 2018” (Australian Bureau of Agricultural and Resource Economics and Sciences, 2018), (available at https://doi.org/10.25814/5bceb32574707).

17. Sydney Water, “Water Conservation Report 2019-2020” (2020), (available at https://www.sydneywater.com.au/content/dam/sydneywater/documents/water-conservation-report.pdf [Accessed 2023-04-11]).

18. M. M. Boer, V. Resco de Dios, R. A. Bradstock, Unprecedented burn area of Australian mega forest fires. Nature Climate Change. **10**, 171–172 (2020).

19. J. P. Evans, X. Meng, M. F. McCabe, Land surface albedo and vegetation feedbacks enhanced the millennium drought in south-east Australia. Hydrology and Earth System Sciences. **21**, 409–422 (2017).

20. C. M. Holgate, A. I. J. M. Van Dijk, J. P. Evans, A. J. Pitman, Geophysical Research Letters, in press, doi:10.1029/2020GL090238.

21. NSW DPI, “NSW State Seasonal Update - January 2018” (ISSN 2202-1795 (Online) Volume 6 Issue 1, 2018), (available at https://www.dpi.nsw.gov.au/__data/assets/pdf_file/0005/800744/nsw-state-seasonal-update-january-2018.pdf).

22. H. Nguyen, M. C. Wheeler, J. A. Otkin, T. Cowan, A. Frost, R. Stone, Using the evaporative stress index to monitor flash drought in Australia. Environmental Research Letters. **14**, 064016 (2019).

23. G. J. van Oldenborgh, F. Krikken, S. Lewis, N. J. Leach, F. Lehner, K. R. Saunders, M. van Weele, K. Haustein, S. Li, D. Wallom, S. Sparrow, J. Arrighi, R. K. Singh, M. K. van Aalst, S. Y. Philip, R. Vautard, F. E. L. Otto, Attribution of the Australian bushfire risk to anthropogenic climate change. Natural Hazards and Earth System Sciences. **21**, 941–960 (2021).

24. P. G. Jarvis, The interpretation of the variations in leaf water potential and stomatal conductance found in canopies in the field. Philosophical Transactions of the Royal Society of London, Biological Sciences. **273**, 593–610 (1976).

25. M. G. De Kauwe, B. E. Medlyn, A. M. Ukkola, M. Mu, M. E. B. Sabot, A. J. Pitman, P. Meir, L. A. Cernusak, S. W. Rifai, B. Choat, D. T. Tissue, C. J. Blackman, X. Li, M. Roderick, P. R. Briggs, Identifying areas at risk of drought-induced tree mortality across South-Eastern Australia. Global Change Biology. **26**, 5716–5733 (2020).

26. H. Clarke, R. H. Nolan, V. R. De Dios, R. Bradstock, A. Griebel, S. Khanal, M. M. Boer, Forest fire threatens global carbon sinks and population centres under rising atmospheric water demand. Nat Commun. **13**, 7161 (2022).

27. AEGIC, “Australian wheat” (2022), (available at https://www.aegic.org.au/wp-content/uploads/2022/09/AEGIC-Grain-Note-wheat-22_LR.pdf).

28. AEGIC, “Australian barley” (2022), (available at https://www.aegic.org.au/wp-content/uploads/2022/09/AEGIC-Grain-Note-Barley_22.pdf).

29. M. Freund, B. J. Henley, D. J. Karoly, K. J. Allen, P. J. Baker, Multi-century cool- and warm-season rainfall reconstructions for Australia’s major climatic regions. Climate of the Past. **13**, 1751–1770 (2017).

30. T. R. Vance, A. S. Kiem, L. M. Jong, J. L. Roberts, C. T. Plummer, A. D. Moy, M. A. J. Curran, T. D. van Ommen, Pacific decadal variability over the last 2000 years and implications for climatic risk. Commun Earth Environ. **3**, 1–9 (2022).

31. D. C. Verdon-Kidd, A. S. Kiem, Nature and causes of protracted droughts in southeast Australia: Comparison between the Federation, WWII, and Big Dry droughts. Geophysical Research Letters. **36** (2009), doi:10.1029/2009GL041067.

32. W. Cai, A. Purich, T. Cowan, P. Van Rensch, E. Weller, Did climate change-induced rainfall trends contribute to the australian millennium drought? Journal of Climate. **27**, 3145–3168 (2014).

33. C. C. Ummenhofer, M. H. England, P. C. McIntosh, G. A. Meyers, M. J. Pook, J. S. Risbey, A. S. Gupta, A. S. Taschetto, What causes southeast Australia’s worst droughts? Geophysical Research Letters. **36**, L04706 (2009).

34. C. C. Ummenhofer, A. S. Gupta, P. R. Briggs, M. H. England, P. C. McIntosh, G. A. Meyers, M. J. Pook, M. R. Raupach, J. S. Risbey, Indian and Pacific Ocean Influences on Southeast Australian Drought and Soil Moisture. Journal of Climate. **24**, 1313–1336 (2011).

35. A. D. King, A. J. Pitman, B. J. Henley, A. M. Ukkola, J. R. Brown, The role of climate variability in Australian drought. Nature Climate Change. **10**, 177–179 (2020).

36. N. Nicholls, Local and remote causes of the southern Australian autumn-winter rainfall decline, 1958-2007. Climate Dynamics. **34**, 835–845 (2010).

37. P. van Rensch, A. J. E. Gallant, W. Cai, N. Nicholls, Evidence of local sea surface temperatures overriding the southeast Australian rainfall response to the 1997–1998 El Niño. Geophysical Research Letters. **42**, 9449–9456 (2015).

38. M. B. Freund, A. G. Marshall, M. C. Wheeler, J. N. Brown, Geophysical Research Letters, in press, doi:10.1029/2020GL091131.

39. G. J. van Oldenborgh, H. Hendon, T. Stockdale, M. L’Heureux, E. C. de Perez, R. Singh, M. van Aalst, Defining El Niño indices in a warming climate. Environ. Res. Lett. **16**, 044003 (2021).

40. H. H. Hendon, D. W. J. Thompson, M. C. Wheeler, Australian Rainfall and Surface Temperature Variations Associated with the Southern Hemisphere Annular Mode. Journal of Climate. **20**, 2452–2467 (2007).

41. E.-P. Lim, H. H. Hendon, G. Boschat, D. Hudson, D. W. J. Thompson, A. J. Dowdy, J. M. Arblaster, Australian hot and dry extremes induced by weakenings of the stratospheric polar vortex. Nat. Geosci. **12**, 896–901 (2019).

42. A. S. Taschetto, M. Stojanovic, C. Holgate, A. Drumond, J. P. Evans, L. Gimeno, R. Nieto, Decline in moisture sources explains the onset and development of the 2017-2019 Murray-Darling Basin Drought (under review).

43. M. J. Pook, P. C. McIntosh, G. A. Meyers, The Synoptic Decomposition of Cool-Season Rainfall in the Southeastern Australian Cropping Region. Journal of Applied Meteorology and Climatology. **45**, 1156–1170 (2006).

44. A. Pepler, Record Lack of Cyclones in Southern Australia During 2019. Geophysical Research Letters. **47** (2020) (available at https://doi.org/10.1029/2020GL088488).

45. T. Parker, A. J. E. Gallant, The role of heavy rainfall in drought in Australia. Weather and Climate Extremes. **38**, 100528 (2022).

46. A. J. E. Gallant, D. J. Karoly, Atypical influence of the 2007 La Niña on rainfall and temperature in southeastern Australia. Geophysical Research Letters. **36** (2009), doi:10.1029/2009GL039026.

47. J. S. Risbey, M. J. Pook, P. C. McIntosh, M. C. Wheeler, H. H. Hendon, On the remote drivers of rainfall variability in Australia. Monthly Weather Review. **137**, 3233–3253 (2009).

48. S. H. Larsen, N. Nicholls, Southern Australian rainfall and the subtropical ridge: Variations, interrelationships, and trends. Geophysical Research Letters. **36**, L08708 (2009).

49. H. Joos, M. Sprenger, H. Binder, U. Beyerle, H. Wernli, Warm conveyor belts in present-day and future climate simulations. Part I: Climatology and impacts. Weather and Climate Dynamics Discussions, 1–30 (2022).

50. BoM, “Australian long-range forecasts archive” (2017), (available at http://www.bom.gov.au/climate/ahead/outlooks/archive.shtml [Accessed 2023-06-13]).

51. S. Hobeichi, G. Abramowitz, J. P. Evans, A. Ukkola, Water Resources Research, in press, doi:10.1029/2021WR031829.

52. A. Devanand, J. P. Evans, G. Abramowitz, S. Hobeichi, A. J. Pitman, What is the probability that a drought will break in Australia? Preprint (2022), doi:https://dx.doi.org/10.2139/ssrn.4251061.

53. M. R. Grose, S. Narsey, F. P. Delage, A. J. Dowdy, M. Bador, G. Boschat, C. Chung, J. B. Kajtar, S. Rauniyar, M. B. Freund, K. Lyu, H. Rashid, X. Zhang, S. Wales, C. Trenham, N. J. Holbrook, T. Cowan, L. Alexander, J. M. Arblaster, S. Power, Insights From CMIP6 for Australia’s Future Climate. Earth’s Future. **8** (2020), doi:10.1029/2019EF001469.

54. A. M. Ukkola, M. G. De Kauwe, M. L. Roderick, G. Abramowitz, A. J. Pitman, Robust Future Changes in Meteorological Drought in CMIP6 Projections Despite Uncertainty in Precipitation. Geophysical Research Letters. **47** (2020), doi:10.1029/2020GL087820.

55. BoM, “State of the Climate 2022” (2022), (available at http://www.bom.gov.au/state-of-the-climate/).

56. H. Douville, K. Raghavan, J. Renwick, R. P. Allan, P. A. Arias, M. Barlow, R. Cerezo-Mota, A. Cherchi, T. Y. Gan, J. Gergis, D. Jiang, A. Khan, W. Pokam Mba, D. Rosenfeld, J. Tierney, O. Zolina, "Water Cycle Changes" in Climate Change 2021: The Physical Science Basis. Contribution of Working Group I to the Sixth Assessment Report of the Intergovernmental Panel on Climate Change [Masson-Delmotte, V., P. Zhai, A. Pirani, S.L. Connors, C. Péan, S. Berger, N. Caud, Y. Chen, L. Goldfarb, M.I. Gomis, M. Huang, K. Leitzell, E. Lonnoy, J.B.R. Matthews, T.K. Maycock, T. Waterfield, O. Yelekçi, R. Yu, and B. Zhou (eds.)], V. Masson-Delmotte, P. Zhai, A. Pirani, S. L. Connors, C. Péan, S. Berger, N. Caud, Y. Chen, L. Goldfarb, M. I. Gomis, M. Huang, K. Leitzell, E. Lonnoy, J. B. R. Matthews, T. K. Maycock, T. Waterfield, O. Yelekçi, R. Yu, B. Zhou, Eds. (Cambridge University Press, Cambridge, United Kingdom and New York, NY, USA, 2021; 10.1017/9781009157896.010), pp. 1055–1210.

57. T. B. McKee, N. J. Doesken, J. Kleist, "The Relationship of Drought Frequency and Duration to Time Scales" in (Anaheim, California, 1993).

58. D. A. Jones, W. Wang, R. Fawcett, High-quality spatial climate data-sets for Australia. Australian Meteorological and Oceanographic Journal. **58**, 233–248 (2009).

59. S. M. Vicente-Serrano, S. Beguería, J. I. López-Moreno, A Multiscalar Drought Index Sensitive to Global Warming: The Standardized Precipitation Evapotranspiration Index. Journal of Climate. **23**, 1696–1718 (2010).

60. A. Frost, A. Ramchurn, A. Smith, The Australian Landscape Water Balance model (AWRA-L v6) Technical Description of the Australian Water Resources Assessment Landscape model version 6 (2018).

61. BoM, "Australian Groundwater Explorer web portal" (2022), (available at http://www.bom.gov.au/water/groundwater/explorer/map.shtml [Accessed 2022-08-06]).

62. M. Ho, A. S. Kiem, D. C. Verdon-Kidd, A paleoclimate rainfall reconstruction in the Murray-Darling Basin (MDB), Australia: 2. Assessing hydroclimatic risk using paleoclimate records of wet and dry epochs. Water Resources Research. **51**, 8380–8396 (2015).

63. T. R. Ault, S. S. George, J. E. Smerdon, S. Coats, J. S. Mankin, C. M. Carrillo, B. I. Cook, S. Stevenson, A Robust Null Hypothesis for the Potential Causes of Megadrought in Western North America. Journal of Climate. **31**, 3–24 (2018).

64. S. Coats, J. E. Smerdon, S. Stevenson, J. T. Fasullo, B. Otto-Bliesner, T. R. Ault, Paleoclimate Constraints on the Spatiotemporal Character of Past and Future Droughts. Journal of Climate. **33**, 9883–9903 (2020).

65. A. Stohl, P. James, A Lagrangian Analysis of the Atmospheric Branch of the Global Water Cycle. Part I: Method Description, Validation, and Demonstration for the August 2002 Flooding in Central Europe. Journal of Hydrometeorology. **5**, 656–678 (2004).

66. L. Gimeno, R. Nieto, A. Drumond, R. Castillo, R. Trigo, Influence of the intensification of the major oceanic moisture sources on continental precipitation. Geophysical Research Letters. **40**, 1443–1450 (2013).

67. L. Gimeno, J. Eiras-Barca, A. M. Durán-Quesada, F. Dominguez, R. van der Ent, H. Sodemann, R. Sánchez-Murillo, R. Nieto, J. W. Kirchner, The residence time of water vapour in the atmosphere. Nat Rev Earth Environ. **2**, 558–569 (2021).

68. R. Nieto, L. Gimeno, A database of optimal integration times for Lagrangian studies of atmospheric moisture sources and sinks. Sci Data. **6**, 59 (2019).

69. M. Sprenger, G. Fragkoulidis, H. Binder, M. Croci-Maspoli, P. Graf, C. M. Grams, P. Knippertz, E. Madonna, S. Schemm, B. Škerlak, H. Wernli, Global Climatologies of Eulerian and Lagrangian Flow Features based on ERA-Interim. Bulletin of the American Meteorological Society. **98**, 1739–1748 (2017).

70. J. S. Risbey, P. C. McIntosh, M. J. Pook, Synoptic components of rainfall variability and trends in southeast Australia. International Journal of Climatology. **33**, 2459–2472 (2013).

71. A. S. Pepler, A. J. Dowdy, P. van Rensch, I. Rudeva, J. L. Catto, P. Hope, The contributions of fronts, lows and thunderstorms to southern Australian rainfall. Clim Dyn. **55**, 1489–1505 (2020).

72. K. A. Browning, Conceptual Models of Precipitation Systems. Weather and Forecasting. **1**, 23–41 (1986).

73. H. Wernli, M. Sprenger, Identification and ERA-15 Climatology of Potential Vorticity Streamers and Cutoffs near the Extratropical Tropopause. Journal of the Atmospheric Sciences. **64**, 1569–1586 (2007).

74. S. Clark, M. j. Reeder, C. Jakob, Rainfall regimes over northwestern Australia. Quarterly Journal of the Royal Meteorological Society. **144**, 458–467 (2018).

75. M. Mu, M. G. De Kauwe, A. M. Ukkola, A. J. Pitman, T. E. Gimeno, B. E. Medlyn, D. Or, J. Yang, D. S. Ellsworth, Evaluating a land surface model at a water-limited site: implications for land surface contributions to droughts and heatwaves. Hydrology and Earth System Sciences. **25**, 447–471 (2021).

76. M. Mu, A. J. Pitman, M. G. De Kauwe, A. M. Ukkola, J. Ge, How do groundwater dynamics influence heatwaves in southeast Australia? Weather and Climate Extremes. **37**, 100479 (2022).

77. A. L. Hirsch, J. Kala, C. C. Carouge, M. G. De Kauwe, G. Di Virgilio, A. M. Ukkola, J. P. Evans, G. Abramowitz, Evaluation of the CABLEv2.3.4 Land Surface Model Coupled to NU-WRFv3.9.1.1 in Simulating Temperature and Precipitation Means and Extremes Over CORDEX AustralAsia Within a WRF Physics Ensemble. Journal of Advances in Modeling Earth Systems. **11**, 4466–4488 (2019).

78. L. Breiman, Random Forests. Machine Learning. **45**, 5–32 (2001).

79. S. P. Rauniyar, S. B. Power, Estimating future rainfall distributions in a changing climate for water resource planning: Victoria, Australia. Clim Dyn. **60**, 527–547 (2023).

80. H. E. Beck, E. F. Wood, M. Pan, C. K. Fisher, D. G. Miralles, A. I. J. M. van Dijk, T. R. McVicar, R. F. Adler, MSWEP V2 Global 3-Hourly 0.1° Precipitation: Methodology and Quantitative Assessment. *Bulletin of the American Meteorological Society*. **100**, 473–500 (2019).

81. C. Funk, A. Verdin, J. Michaelsen, P. Peterson, D. Pedreros, G. Husak, A global satellite-assisted precipitation climatology. *Earth System Science Data*. **7**, 275–287 (2015).

82. J. Du, J. S. Kimball, "Daily Global Land Surface Parameters Derived from AMSR-E and AMSR2, Version 3." (NASA National Snow and Ice Data Center Distributed Active Archive Center, Boulder, Colorado, USA, 2022), (available at http://dx.doi.org/10.5067/JIKQZ6WO5C5M. [Accessed 2022-10-31]).

83. K. Didan, "MODIS/Aqua Vegetation Indices 16-Day L3 Global 1km SIN Grid V061" (NASA EOSDIS Land Processes DAAC, 2021), (available at https://doi.org/10.5067/MODIS/MYD13A2.061 [Accessed 2022-10-31]).

84. Z. Wan, S. Hook, G. Hulley, "MYD11A1 MODIS/Aqua Land Surface Temperature/Emissivity Daily L3 Global 1km SIN Grid V006" (NASA EOSDIS Land Processes DAAC, 2015), (available at https://doi.org/10.5067/MODIS/MYD11A1.006 [Accessed 2022-10-31]).

85. B. Martens, D. G. Miralles, H. Lievens, R. van der Schalie, R. A. M. de Jeu, D. Fernández-Prieto, H. E. Beck, W. A. Dorigo, N. E. C. Verhoest, GLEAM v3: satellite-based land evaporation and root-zone soil moisture. *Geoscientific Model Development*. **10**, 1903–1925 (2017).

86. B. D. Tapley, S. Bettadpur, M. Watkins, C. Reigber, The gravity recovery and climate experiment: Mission overview and early results. *Geophysical Research Letters*. **31** (2004), doi:10.1029/2004GL019920.

87. B. Huang, P. W. Thorne, V. F. Banzon, T. Boyer, G. Chepurin, J. H. Lawrimore, M. J. Menne, T. M. Smith, R. S. Vose, H.-M. Zhang, "NOAA Extended Reconstructed Sea Surface Temperature (ERSST), Version 5." (NOAA National Centers for Environmental Information, 2017), (available at doi:10.7289/V5T72FNM. Obtain at NOAA/ESRL/PSD at their website https://www.esrl.noaa.gov/psd/).

88. M. Ishii, A. Shouji, S. Sugimoto, T. Matsumoto, Objective analyses of sea-surface temperature and marine meteorological variables for the 20th century using ICOADS and the Kobe Collection. *International Journal of Climatology*. **25**, 865–879 (2005).

89. D. P. Dee, S. M. Uppala, A. J. Simmons, P. Berrisford, P. Poli, S. Kobayashi, U. Andrae, M. A. Balmaseda, G. Balsamo, P. Bauer, P. Bechtold, A. C. M. Beljaars, L. van de Berg, J. Bidlot, N. Bormann, C. Delsol, R. Dragani, M. Fuentes, A. J. Geer, L. Haimberger, S. B. Healy, H. Hersbach, E. V. H??lm, L. Isaksen, P. K??llberg, M. K??hler, M. Matricardi, A. P. Mcnally, B. M. Monge-Sanz, J. J. Morcrette, B. K. Park, C. Peubey, P. de Rosnay, C. Tavolato, J. N. Th??paut, F. Vitart, The ERA-Interim reanalysis: Configuration and performance of the data assimilation system. *Quarterly Journal of the Royal Meteorological Society*. **137**, 553–597 (2011).

Acknowledgments

This research was undertaken with the assistance of resources and services from the National Computational Infrastructure (NCI), which is supported by the Australian Government.

Funding: This work was supported by
Australian Research Council Centre of Excellence for Climate Extremes CE170100023 (AD, GMF, SH, CMH, CJ, MM, TP, SWR, KSR, EV, NJA, GA, JPE, AJEG, AJP, AST, AMU)
Xunta of Galicia (regional government) Grant no. ED481B-2021/134 (MS)
Australian Research Council Discovery Early Career Award DE200100086 (AMU)
Australian Government's National Environmental Science Program, Community Grants Program, Activity ID 4-G47AV4M (NJA, JPE, AJEG, SPR)

Author contributions:
Conceptualization: AD, GMF, ZEG, SH, CMH, TP, SWR, NJA, GA, JPE, AJEG, AJP, AST, AMU
Methodology: AD, GMF, ZEG, SH, CMH, CJ, MM, TP, SWR, KSR, MS, EV, NJA, GA, SC, JPE, AJEG, AJP, SBP, SPR, AST
Formal analysis: AD, GMF, ZEG, SH, CMH, CJ, MM, TP, SWR, KSR, MS, EV, NJA, SC, SPR, AST
Visualization: AD, GMF, ZEG, SH, CJ, MM, TP, SWR, MS, EV, NJA, SPR, AST
Writing—original draft: AD, GMF, ZEG, SH, CMH, CJ, MM, TP, SWR, KSR, EV, NJA, GA, JPE, AJEG, AJP, SBP, SPR, AST, AMU
Writing—review & editing: AD, GMF, ZEG, SH, CMH, CJ, MM, TP, SWR, EV, NJA, GA, SC, JPE, AJEG, AJP, SBP, SPR, AST, AMU
Project Administration: AD, AJP

Competing interests: Authors declare they have no competing interests.

Data and materials availability: The sources of the publicly available data used for analyses are listed in Table S1. Simulated datasets will be made available in a zenodo repository on acceptance of the paper. The code is available at https://github.com/anjanadevanand/Tinderbox_drought.

Science Advances
AAAS

Supplementary Materials for

Australia's Tinderbox Drought: an extreme natural event likely worsened by human-caused climate change

Anjana Devanand *et al.*

*Corresponding author. Email: anjana.devanand@unsw.edu.au

This PDF file includes:

Supplementary Text
Figs. S1 to S12
Tables S1 to S3
References (80 to 89) (these refer only to references in the SM)

Supplementary Text

Metrics of Performance of the Random Forest (RF) drought indicator

Random Forest was trained on 750 samples and tested out-of-sample on 187 samples across 50 different sub-sampling schemes. The metrics of performance include:

- Accuracy: The fraction of correct predictions out of all predictions
- Recall: The number of drought predictions expressed as a fraction of observed drought events
- Precision: the fraction of droughts the model identifies correctly out of all drought predictions
- False negative rate: the number of missed ‘drought’ expressed as a fraction of all observed drought events
- F1 score: The harmonic mean of precision and recall expressed as: $F1 = 2 * \frac{Precision * Recall}{Precision + Recall}$
- False alarm rate: the number of incorrect drought predictions expressed as a fraction of all drought predictions.
- A perfect score is 1 for “Accuracy”, “Recall”, “F1 score”, and “Precision” and 0 for “False alarm rate”, and “False negative rate”.

The performance of RF at the testing dataset shows that the RF achieved above 90% accuracy, recall, precision and F1 score across the majority of iterations. False alarm rate (when the RF incorrectly classified a non drought event as a drought) and the False negative rate (when the RF missed a drought event) were also below 10% (Supplementary figure 12b)).

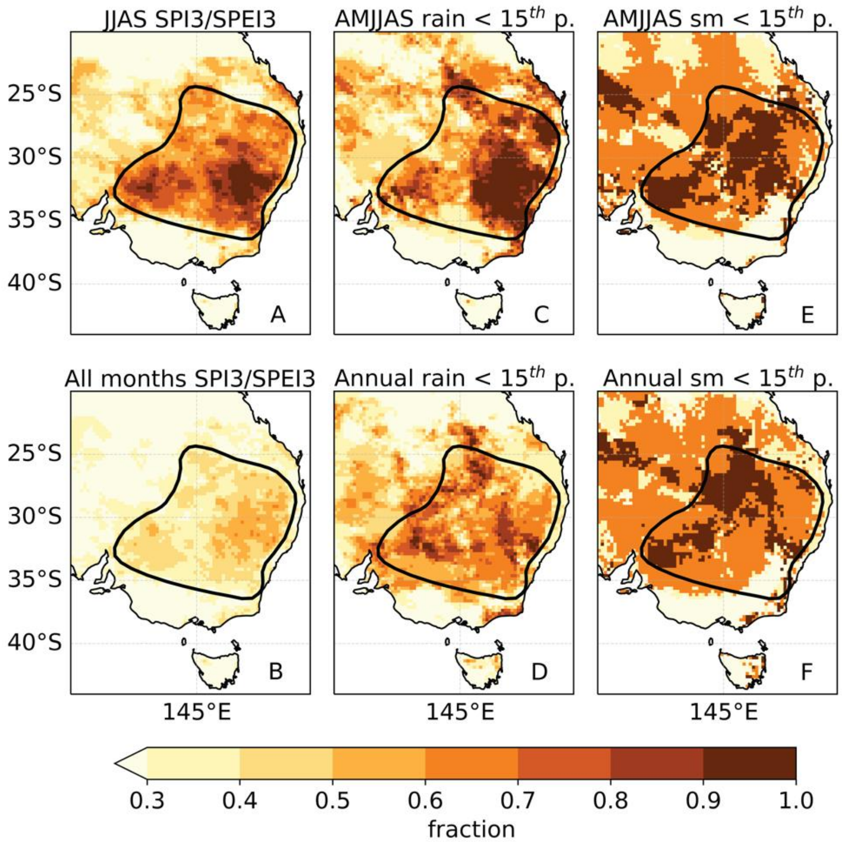

Fig. S1. The proportion of time in drought based on various metrics and the focus region for analysis. (**A-B**) the mean proportion of time SPI-3/SPEI-3 ≤ -1 during JJAS 2017-19 and all months 2017-19 based on three precipitation and two PET datasets, (**C-D**) the mean proportion of time during which the AMJJAS total and annual precipitation are below the corresponding 15th percentile thresholds based on three precipitation datasets, and (**E-F**) the mean proportion of time during which the AMJJAS and annual mean soil moisture form the ESACCI dataset are below the corresponding 15th percentile thresholds. A reference period of 1980-01 to 2016-12 is used to calculate SPI-3/SPEI-3 and the percentile thresholds. Thick black line on each panel shows the drought area.

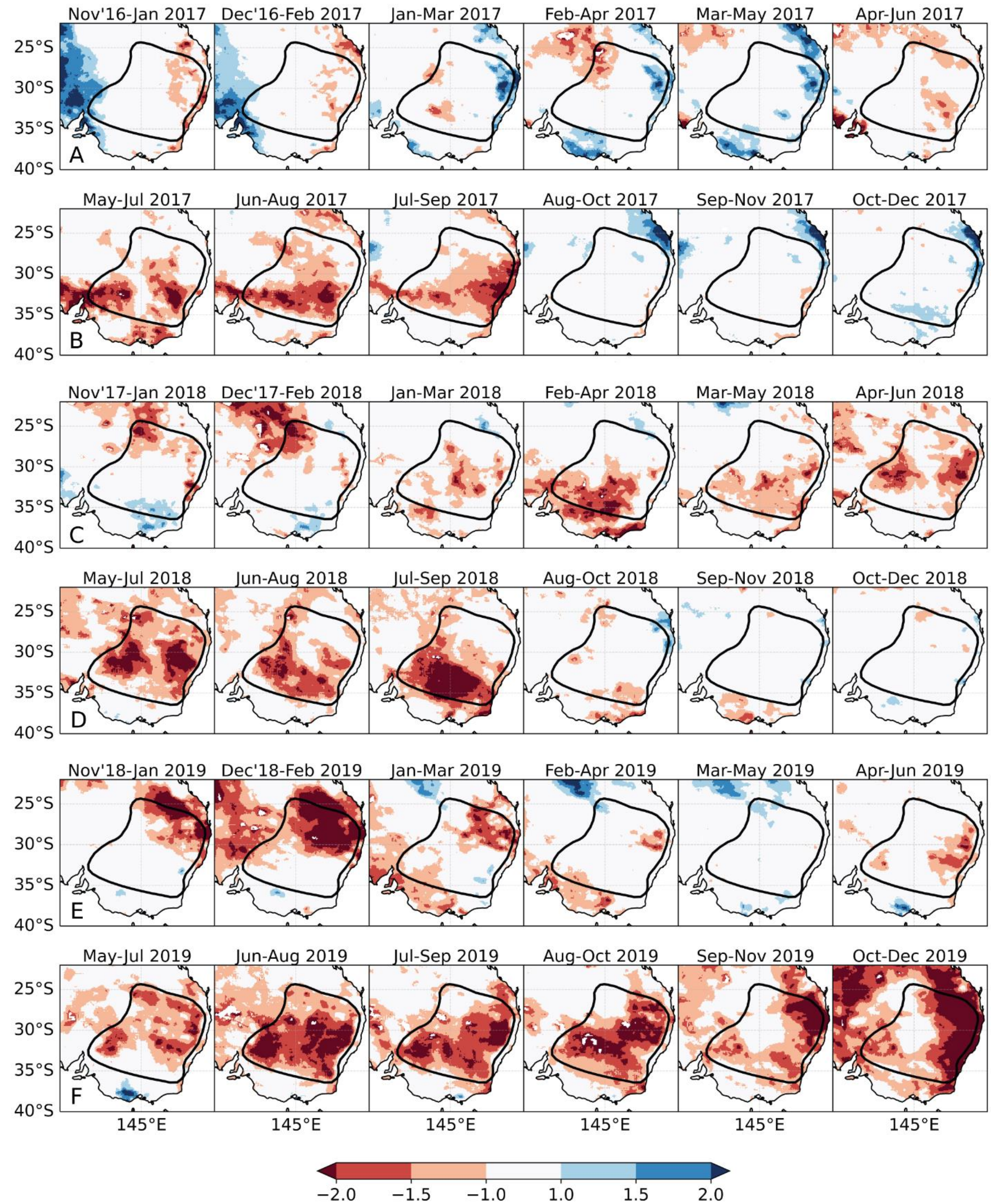

Fig. S2. Mean SPI-3 during 2017-19 estimated from AGCDv1, MSWEP, and CHIRPS precipitation datasets. Thick black line on each panel shows the drought area.

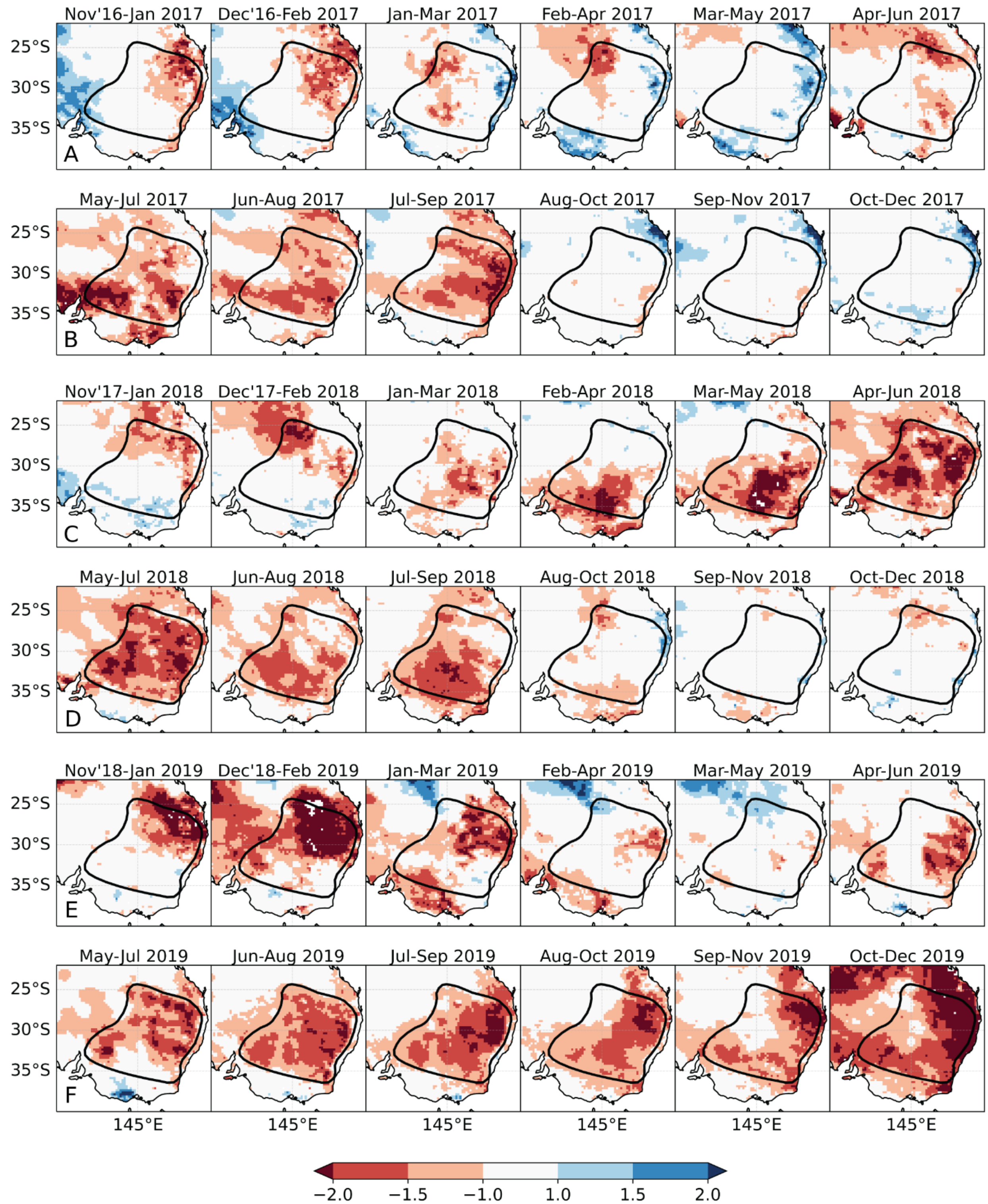

Fig. S3. Mean SPEI-3 during 2017-19 estimated from AWRA-AGCDv1 and GLEAM-MSWEP datasets. Thick black line on each panel shows the drought area.

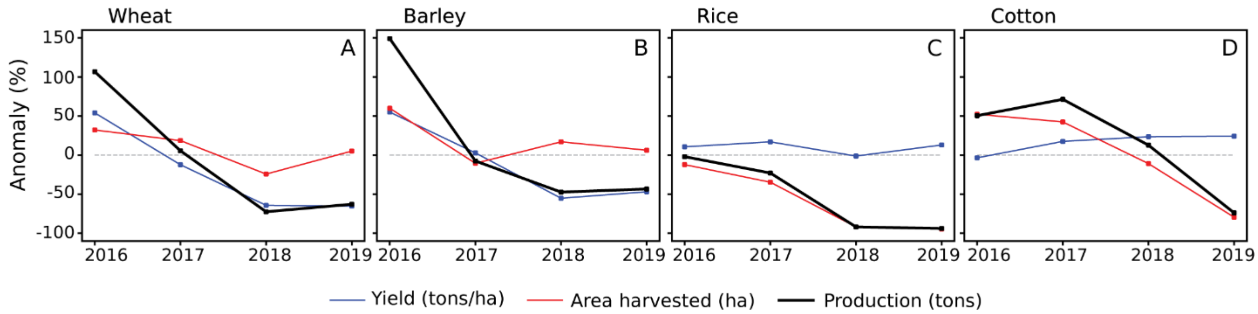

Fig. S4. Agricultural production, yield and area harvested from 2016 to 2019 for (**A**) wheat, (**B**) barley, (**C**) rice and (**D**) cotton. All time series are presented as anomalies (in percent) from the long-term average computed over the years 1990-2016. Yields (blue line) are defined as the production for a given crop per area harvested (reported in tons per hectare); area harvested refers to the land area from which a crop was harvested (in hectares), and production is the product of yield and area harvested (in tons). The wheat and barley statistics are derived from the ABARES farm survey data at sub-national scale, for regions affected by the drought, whereas the rice and cotton statistics are derived from the FAOSTAT database at the national scale for Australia. Please note, rice and cotton are summer crops with a growing season ranging from Southern Hemisphere spring to autumn, spanning two calendar years. For these crops, this figure presents agricultural statistics for the year in which the growing season starts. For example, the 2018 data point for rice and cotton describes the 2018-19 growing season.

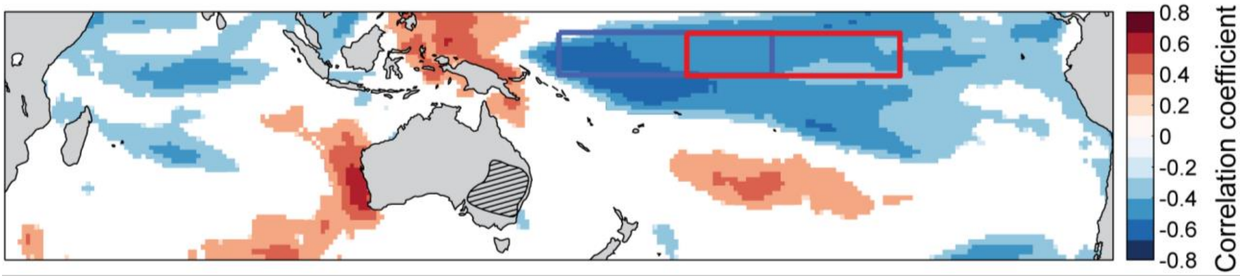

Fig. S5. Spatial correlation of warm season (October-March) rainfall anomalies in our study region (hatching) with SST anomalies, showing only correlations significant at $p < 0.1$, similar to that shown in Figure 5A for the cool season. Data in this figure uses the OISST v2 0.25°×0.25° SST product and the ACGD rainfall product between 1982-2020, linearly detrended to emphasise interannual variability. Blue rectangle denotes Niño4 region; red rectangle denotes Niño3.4 region.

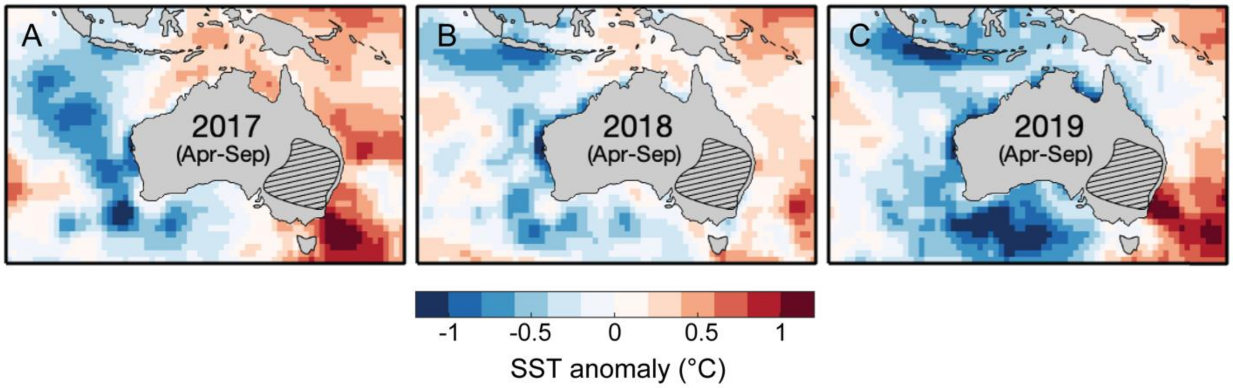

Fig. S6. SST anomalies around Australia for April-September of the Tinderbox drought years. Data in this figure uses the OISST v2 0.25°×0.25° SST product linearly detrended to emphasise interannual variability, and anomalies in are relative to 1982-2016 climatology (Methods)

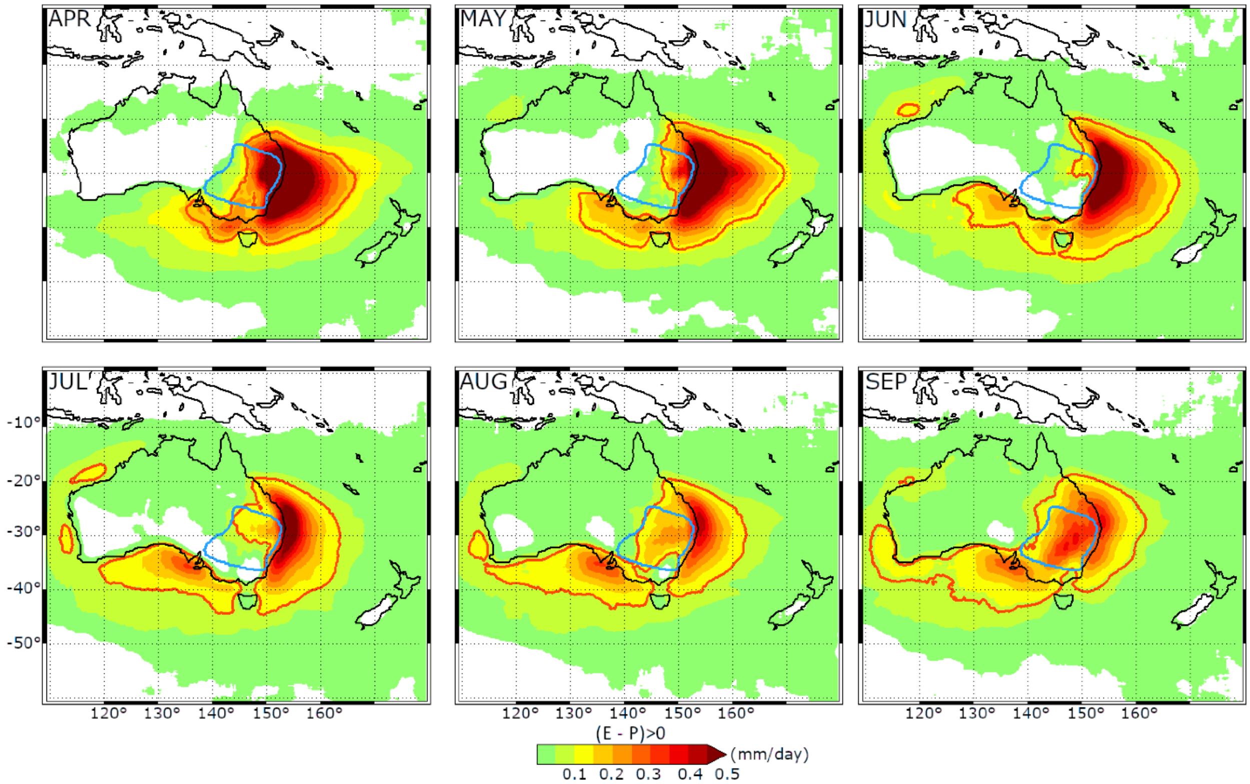

Fig. S7. Climatological cool season (AMJJAS) moisture source (E-P>0) for the Tinderbox Drought region (blue line) obtained from the backward experiment based on ERA-Interim from 1980 to 2016. The red line encompasses 95% of the moisture source to the Tinderbox Drought region.

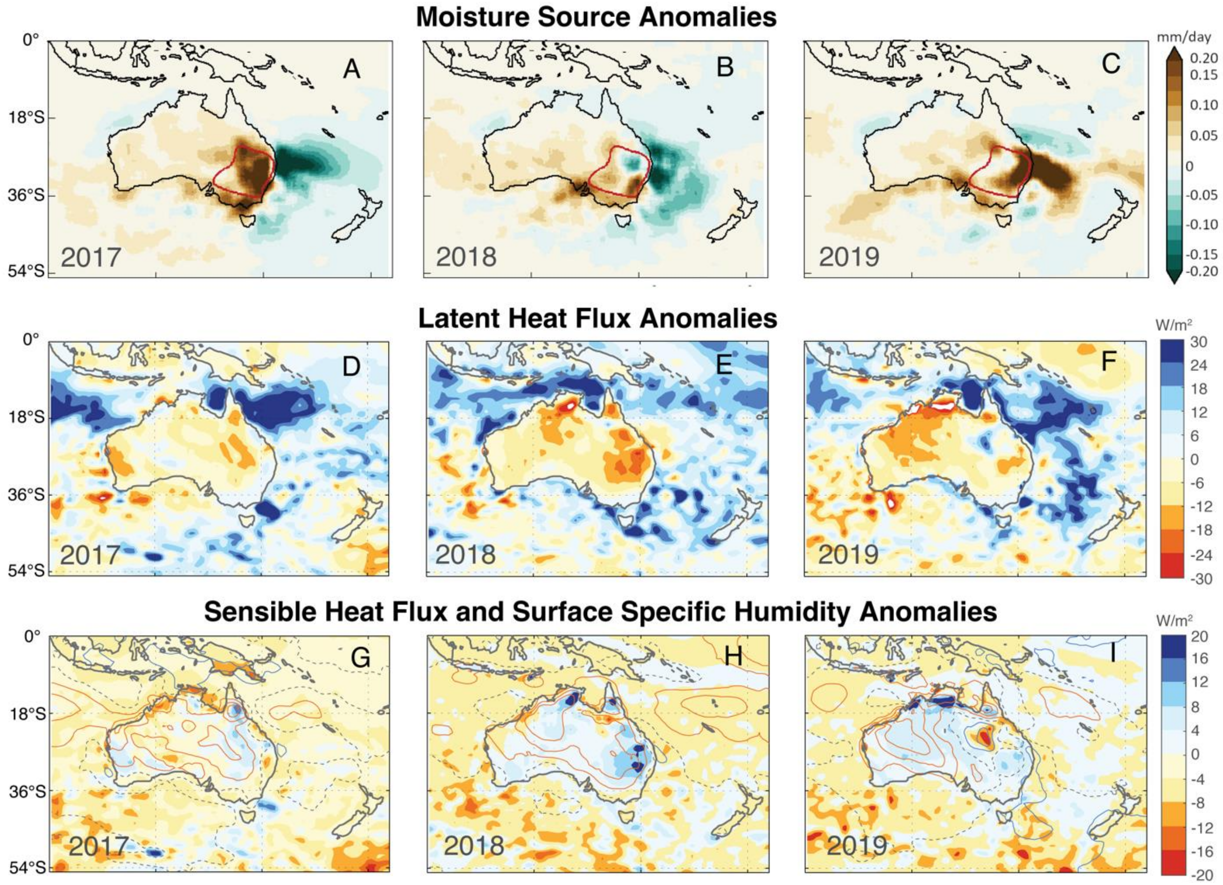

Fig. S8. Anomalies of (**A,B,C**) moisture source (mm/day), (**D,E,F**) latent heat flux (W/m^2), (**G,H,I**) sensible heat flux (W/m^2, shading) and specific humidity (kg/kg, contours). Anomalies are calculated relative to April-to-July 1980-2016 climatology from April to July for (**A,D,G**) 2017 (**B,E,H**) 2018, and (**C,F,I**) 2019 relative to April-to-July 1980-2016 climatology. Note that the analysis uses a shorter cool season (April to July) due to ERA-Interim data availability (stops in Aug 2019). April-to-September anomalies for 2017 and 2018 can be seen in Fig. S9.

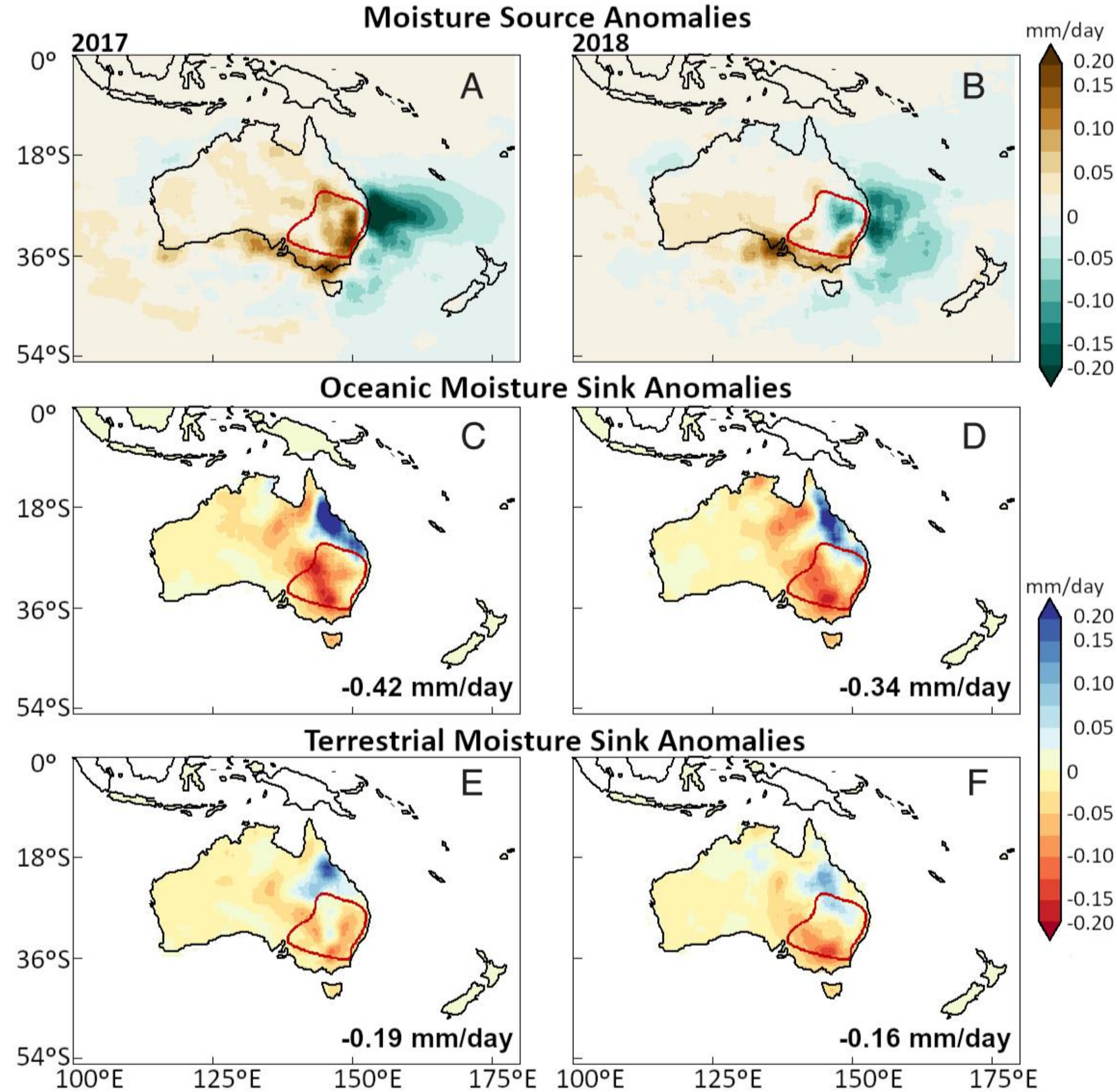

Fig. S9. Anomalies of **(A,B)** moisture source (mm/day), **(C,D)** oceanic moisture sink (mm/day), **(E,F)** terrestrial moisture sink (mm/day), from April to September for **(A,C,E)** 2017 and **(B,D,F)** 2018, relative to April-to-September 1980-2016 climatology.

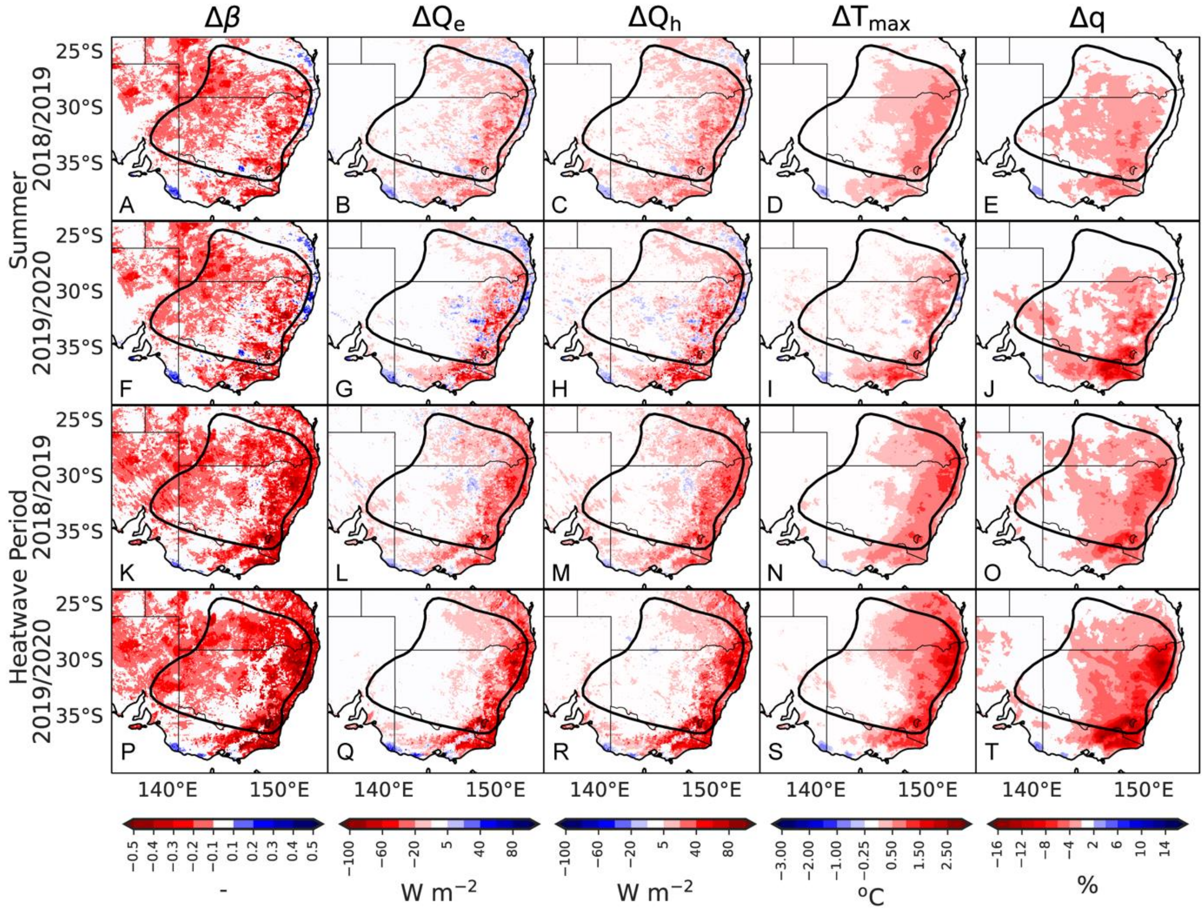

Fig. S10. The impact of soil moisture drought on the 2018/2019 and 2019/2020 summers (DJF) and on the heatwave periods of 14-26 Jan 2019 and of 16 Dec 2019-7 Jan 2020. The left column is the WRF-CABLE simulated difference in the soil water stress factor ($\Delta\beta$, DROUGHT– CLIM). A negative value indicates an increase of water stress on plant transpiration due to the root zone moisture deficit during the drought. The 2nd and 3rd columns are the differences in the surface latent heat flux (ΔQe, W/m^2) and sensible heat flux (ΔQh, W/m^2), and right two columns are the difference in maximum air temperature (ΔTmax, ºC) and the percentage rate of specific humidity changes (Δq, %). The black polygon highlights the drought area.

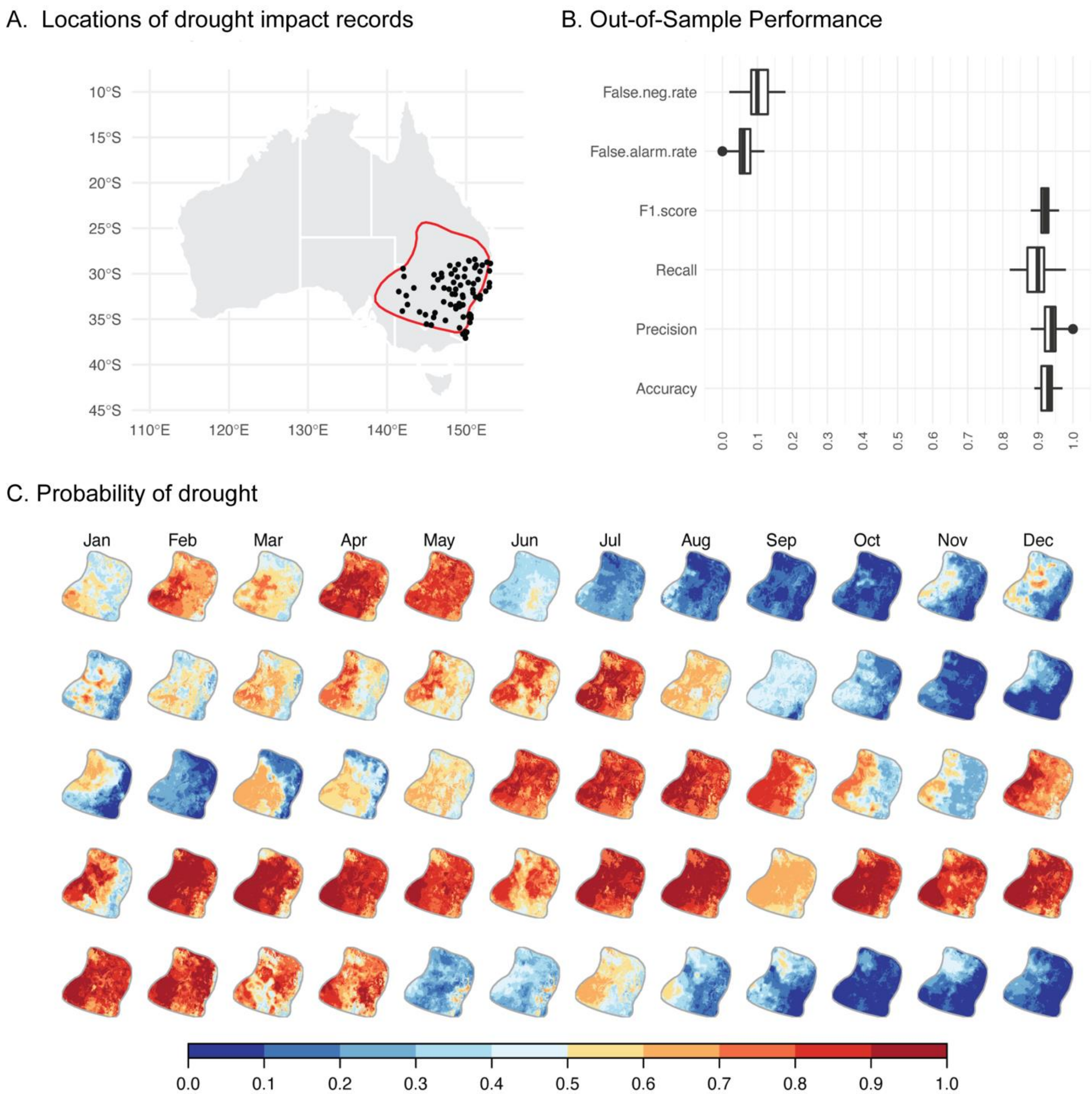

Fig. S11. **(A)** Map showing the location of drought impact records (black) and the region of interest (red); **(B)** Performance of the Random Forest indicator at testing samples across 50 different sub-sampling of training and testing samples. Performance metrics are explained in Supplementary Text 1; **(C)** Spatial distribution of the temporal evolution of drought probability during 2016 – 2020.

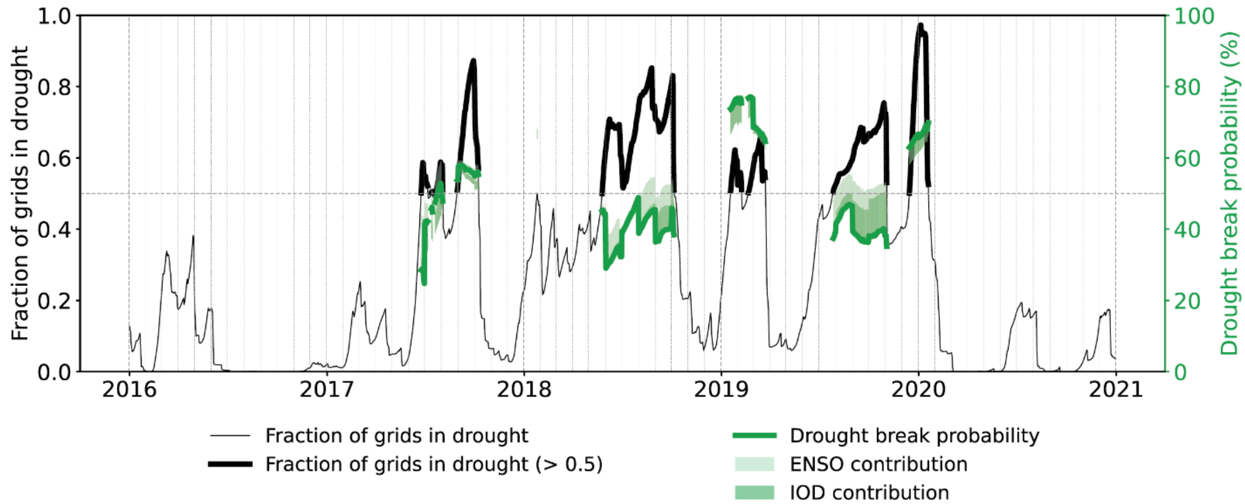

Fig. S12. Drought breaking probabilities during the Tinderbox Drought. Fraction of grids in the drought focus region experiencing soil moisture drought (light blue and black; black indicates fraction > 0.5), area average probability of the drought-breaking in 8 weeks (green line) during periods when more than 50% of the grids experienced drought, and the contributions of ENSO and IOD to drought-breaking probabilities (light and dark green shading).

Table S1. Datasets used for analyses

	Datasets	Time period
Precipitation, Temperature, Vapour Pressure	Australian Gridded Climate Data version 1 (AGCD) http://www.bom.gov.au/climate/austmaps/metadata-monthly-rainfall.shtml http://www.bom.gov.au/climate/austmaps/metadata-daily-rainfall.shtml	1900 to 2020
Precipitation	Multi-Source Weighted Ensemble Precipitation (MSWEPv2.8) http://www.gloh2o.org/mswep/ (*80*)	1979 to 2020
	Climate Hazards Group InfraRed Precipitation with Station data (CHIRPS-2.0) https://www.chc.ucsb.edu/data/chirps (*81*)	1981 to 2020
Soil Moisture	ESA CCI SM v06.1 https://esa-soilmoisture-cci.org	1978 to 2020
	OzFlux observation network https://ozflux.org.au	2002 to 2020
Vegetation	Vegetation Optical Depth using the LPDR v3 product (*82*) http://files.ntsg.umt.edu/data/LPDR_v3/GeoTif Normalized Difference Vegetation Index from MYD13A2 collection 6.1 (*83*) https://lpdaac.usgs.gov/products/myd13a2v061/ Land Skin Temperature at 13:30 from MODIS AQUA from the MYD11A1 collection 6.1 product (*84*) https://lpdaac.usgs.gov/products/myd11a1v061/	2002 to 2020
Evaporation, Potential Evapotranspiration	Australian Water Resources Assessment Landscape (AWRA-L) model http://www.bom.gov.au/water/landscape/	1911 to 2020
	Global Land Evaporation Amsterdam Model (GLEAMv3.5) https://www.gleam.eu (*85*)	1981 to 2020
Terrestrial Water Storage	GRACE MASCON data, NASA Jet Propulsion Laboratory (*86*) https://grace.jpl.nasa.gov/data/get-data/jpl_global_mascons/	2003 to 2020
Streamflow	Bureau of Meteorology Hydrologic Reference Stations (HRS) http://www.bom.gov.au/water/hrs/	various
Bore well water levels	Bureau of Meteorology Australian Groundwater Explorer http://www.bom.gov.au/water/groundwater/explorer/map.shtml	various
Indices of ENSO	Monthly Niño 3.4 SST time series from NOAA https://psl.noaa.gov/data/timeseries/monthly/NINO34/ Nino4 https://psl.noaa.gov/data/timeseries/monthly/NINO4/ SOI http://www.bom.gov.au/climate/enso/soi/ Relative ENSO SST indices using ERSST *(39)*	1950 to 2022
Indices of IOD	https://psl.noaa.gov/gcos_wgsp/Timeseries/DMI/	1870 to 2022
Indices of SAM	https://legacy.bas.ac.uk/met/gjma/sam.html	1957 to 2022
Agricultural impacts	ABARES farm survey data: https://www.awe.gov.au/abares/data/farm-data-portal#data-download ABS agricultural statistics FAOSTAT: https://www.fao.org/faostat/en/#data/QCL	1990-2020 2007/08 - 2019/20 1961-2020
Atmospheric boundary layer characteristics	ECMWF Reanalysis v5 (ERA5)	2017-2020
Sea surface temperature	OISST v2 1x1 degree resolution and 0.25x0.25 degree resolution products https://psl.noaa.gov/data/gridded/data.noaa.oisst.v2.html https://psl.noaa.gov/data/gridded/data.noaa.oisst.v2.highres.html NOAA Extended Reconstructed SST V5 (*87*): https://psl.noaa.gov/data/gridded/data.noaa.ersst.v5.html COBE SST (*88*): https://psl.noaa.gov/data/gridded/data.cobe.html	1982-2022 1900-2016 1900-2016

Weather feature dataset	http://eraiclim.ethz.ch/	1980-2019
Moisture sources	ERA-Interim - European Centre for Medium-Range Weather Forecasts (ECMWF) Reanalysis (*89*) https://www.ecmwf.int/en/forecasts/datasets/reanalysis-datasets/era-interim.	1980-2019

Table S2. Monthly optimal integration time of water vapour for Australia during the cool season months.

Months	Days
Apr	6
May	7
Jun	8
Jul	8
Aug	8
Sep	9

Table S3. Details of CMIP6 models used in this study. Only the first ensemble run (i.e., r1i1p1f1) is being used in this study. There are 31 models that are common across pre-industrial runs with at least 200 years of simulations, historical (1900 – 2014) simulations under all-forcing (natural + anthropogenic) and future (2015 – 2100) projections under SSP5.85 scenario. Models shown in bold have future projections (2015 – 2100) missing under other scenarios.

Model Names	**piControl**	**Historical**	**Future Scenarios**				**Atmospheric grid lat/lon resolution**
	200 years	**ALL-forcing**	**SSP5.85**	**SSP3.70**	**SSP2.45**	**SSP1.26**	
ACCESS-CM2	1	1	1	1	1	1	1.2 × 1.8
ACCESS-ESM1-5	1	1	1	1	1	1	1.2 × 1.8
AWI-CM-1-1-MR	1	1	1	1	1	1	0.9 × 0.9
BCC-CSM2-MR	1	1	1	1	1	1	1.1 × 1.1
CanESM5	1	1	1	1	1	1	2.8 × 2.8
CAS-ESM2-0	1	1	1	1	1	1	1.4 × 1.4
CESM2-WACCM	1	1	1	1	1	1	0.9 × 1.25
CESM2	1	1	1			1	~1.0
CIESM	1	1	1		1	1	1.0 × 1.0
CMCC-CM2-SR5	1	1	1	1	1	1	~0.9
CMCC-ESM2	1	1	1	1	1	1	0.9 × 1.25
EC-Earth3	1	1	1	1	1	1	0.7 × 0.7

EC-Earth3-CC	1	1	1		1		~1.0
EC-Earth3-Veg	1	1	1	1	1	1	0.7 × 0.7
EC-Earth3-Veg-LR	1	1	1	1	1	1	0.7 × 0.7
FGOALS-f3-L	1	1	1	1	1	1	2.3 × 2.0
FGOALS-g3	1	1	1	1	1	1	2.3 × 2.0
GFDL-CM4	1	1	1		1		1.0 × 1.3
GFDL-ESM4	1	1	1	1	1	1	1.0 × 1.3
INM-CM4-8	1	1	1	1	1	1	1.5 × 2.0
INM-CM5-0	1	1	1	1	1	1	1.5 × 2.0
IPSL-CM6A-LR	1	1	1	1	1	1	1.3 × 2.5
KACE-1-0-G	1	1	1	1	1	1	1.25 × 1.87
MIROC6	1	1	1	1	1	1	1.4 × 1.4
MPI-ESM1-2-HR	1	1	1	1	1	1	~0.9
MPI-ESM1-2-LR	1	1	1	1	1	1	~2.0
MRI-ESM2-0	1	1	1	1	1	1	1.1 × 1.1
NESM3	1	1	1		1	1	1.9 x 1.9
NorESM2-LM	1	1	1	1	1	1	0.9 × 0.9

NorESM2-MM	1	1	1	1	1	1	0.9 × 0.9
TaiESM1	1	1	1	1	1	1	0.9 × 0.9
Total	**31**	**31**	**31**	**28**	**30**	**29**	